

# Nebular Abundances in Star-Forming Dwarf Galaxies

by

Matthew D. Johnson

Class of 2007

A thesis submitted to the  
faculty of Wesleyan University  
in partial fulfillment of the requirements for the  
Degree of Bachelor of Arts  
with Departmental Honors in Astronomy

# Acknowledgments

One of the lessons I have learned in my four years at Wesleyan is that in the sciences (and, perhaps, in life) one can never accomplish very much without the help and support of one's peers and mentors. To that end, I would like to begin by thanking my advisor, John Salzer, for his time and enthusiasm throughout this project. His belief in the ability of undergraduates to do real, legitimate research has been unflagging, and that has been very encouraging indeed. I would also like to thank Bill Herbst, Kathryn Johnston and Ed Moran, all of whom have been extremely supportive and available, and who have often gone well above and beyond the call of duty on behalf of their students.

I am also deeply indebted to all the people who have worked on ELSA. Although it was originally my own brainchild, there is no way it would have become what it is today without the tireless efforts of Karen Kwitter and Richard Henry, who introduced me to the world of chemical abundances and kept me in line when the cynical programmer half of my brain threatened to overcome the thoughtful scientist half. I also am extremely grateful to my programming partners in crime: Jesse Levitt, Peter O'Malley and Peter Nunns.

I also want to thank all my fellow astronomy and physics majors, who are too numerous to name here. The road I've walked would've been so much lonelier without all of you.

Finally, I thank my family for believing in me, and for all they have done for me to make my education to this point possible. They encouraged me, quite literally, to reach for the stars.

# Contents

<b>1</b>	<b>Introduction</b>	<b>1</b>
1.1	Emission Lines and Chemical Abundances . . . . .	1
1.2	A Volume Density Experiment . . . . .	5
1.3	Reworking the Abundances Data Pipeline . . . . .	6
1.4	Motivation and Goals . . . . .	10
<b>2</b>	<b>Scientific Background</b>	<b>11</b>
2.1	Astrophysical Objects of Interest and the Strömgren Sphere . . . . .	11
2.2	Formation of Recombination Lines . . . . .	13
2.3	Formation of Forbidden Lines . . . . .	16
2.4	Forbidden Line Sensitivity to Temperature and Density . . . . .	20
2.5	Deriving Abundances from Line Strengths . . . . .	25
2.6	Dust and Stellar Absorption . . . . .	26
<b>3</b>	<b>The ELSA Software Package</b>	<b>29</b>
3.1	Synopsis . . . . .	29
3.2	Temperature and Density Calculations . . . . .	31
3.3	Reddening and Absorption Corrections . . . . .	34

3.4	Abundance Calculations . . . . .	40
3.5	Error Propagation . . . . .	45
3.6	Limitations of ELSA . . . . .	49
<b>4</b>	<b>Nebular Abundances of KISS Dwarf Galaxies</b>	<b>51</b>
4.1	Objectives . . . . .	51
4.2	Candidate Galaxy Selection Criteria . . . . .	53
4.3	Data Reductions and Processing . . . . .	56
4.4	Nebular Abundances From ELSA . . . . .	59
4.5	Comparison of ELSA with Prior Results . . . . .	66
<b>5</b>	<b>The Volume Density-Abundance Relationship</b>	<b>68</b>
5.1	The Coarse Abundance Method . . . . .	68
5.2	Determining Volume Density . . . . .	71
5.3	Results . . . . .	75
5.4	Discussion . . . . .	78
<b>6</b>	<b>Conclusion</b>	<b>81</b>
	<b>References</b>	<b>84</b>

# Chapter 1

## Introduction

### 1.1 Emission Lines and Chemical Abundances

The study of spectroscopic emission lines has long been a major area of research in the field of astronomy. Emission lines help us understand the internal processes of a diverse range of astronomical objects which share similar physical properties. All emission lines ultimately result from some process which decreases the energy of an atom or molecule in the source object. As we will see, each line can actually be associated (in most cases) with a specific element, and a specific ionization stage of that element. Emission lines are therefore intrinsically linked to the dynamic behavior of atoms and molecules in objects we observe. Thus, with a thorough treatment of the atomic physics which led to the creation of the lines we observe, we can derive a wealth of information about a variety topics regarding the chemical evolution and nuclear processes of astrophysical objects.

Fundamentally, emission lines are discrete peaks in the flux spectrum of an

astrophysical object. The peaks result from a larger number of photons detected (relative to the background continuum level) at these specific wavelengths. These photons are produced by downward transitions of bound electrons in the atomic population within the object of interest. When electrons in an excited state move to a lower-energy state, they emit photons with an energy equal to the difference between the energies of the two states involved in the transition. The energy of a photon is given as  $E = hc/\lambda$ . Thus, a transition between any two distinct atomic quantum states has a very specific wavelength of light associated with it. A high occurrence of a certain transition in turn produces the flux peaks at specific wavelengths that may be observed in the spectrum of an object.

One of the more interesting results that may be obtained using these emission lines, and the result on which much of this thesis will focus, is the determination of the chemical abundance ratios of photoionized objects. In these objects, a region of gaseous material denser than the normal interstellar or intergalactic medium is exposed to high-energy photons, causing ionization and excitation of the constituent atoms. Occasionally, one of the free (ionized) electrons will “collide” with an ion of a heavier element, exciting it into a so-called “metastable” state – one whose de-excitation via emitting a photon violates atomic selection rules. The density of these objects is typically so low that metastable states generally avoid being de-excited by another collision long enough to radiate so-called “forbidden lines.” It is these lines that enable much of the chemical abundance work we are able to do. The chemical abundances of these objects are often referred to as “nebular abundances” since the astronomical term “nebula” refers to hot, gaseous regions much like the ones under consideration here.

The observed emission line spectra of these objects allows us to reconstruct, using our understanding of quantum mechanics, the relative levels of various elements present in them. This is done by establishing a model of the atom using a finite number of energy levels. In theory, of course, there are an infinite number of energy levels. However, given the types of conditions encountered in actual nebulae, excitations to the very high energy levels become extremely improbable compared to the probability of ionization, so a relatively modest number of allowed energy levels will suffice. Five is a common choice for this parameter. The probability of a transition occurring also depends to a significant degree upon the temperature and density of the environment. These two quantities are very critical parameters. Their determination has a great effect on the final results of an abundance study, and so we will revisit methods of determining them frequently. To find the temperature or density, we typically look at the ratio of two emission lines representing two different transitions within the same ionization stage of a certain element which is particularly sensitive to either temperature or density.

Once all the model parameters are known, we may determine the relative abundance of many different elements (usually with respect to hydrogen, the most abundant element) implied by the strength of various emission lines that we know to be produced by transitions downward from excited states of that element. Usually these known lines are associated not just with certain elements, but certain ionization stages of those elements. We often determine the abundance of ionization stages individually and simply add them up to obtain the total abundance of that element.

It is worth mentioning here that astronomers who work in areas dealing with

chemical abundances have developed a somewhat odd vernacular for discussing the chemical elements. Since truly heavy elements are so rare in the Universe compared to lighter elements, the “heaviest” elements we tend to deal with in abundance studies are on the order of carbon, oxygen, neon and argon. In astronomy these have come to be known as the “metals.” Oxygen is generally a good surrogate for discussing general abundance trends of all elements heavier than hydrogen and helium, so objects with high oxygen abundance are often said to be “metal-rich” while those with low oxygen abundance are “metal-poor.” This language may be somewhat disconcerting to readers who are used to the widely accepted chemistry definition of “metal.” However, in deference to the large amount of astronomical literature that uses this conception of metallicity, this thesis will adopt that nomenclature.

Chemical abundances have a number of useful applications within astronomy. The life cycle of stars, which is at the heart of a large fraction of astrophysical phenomena, is very closely tied to the synthesis of lighter elements into heavier, more complex ones. Thus, deriving the relative abundances of the chemical elements in an astrophysical object is critical to gaining insight into its formation history and structure. This holds for a wide range of nebula-like objects. For example, nebular abundance studies are often carried out on objects ranging from planetary nebulae (medium-mass star ejecta) to active galactic nuclei (high-luminosity galaxy centers). At the same time, an entirely analogous process is used to obtain abundances of an entire compact star-forming dwarf *galaxy*. The physics used to model photoionized gas applies to essentially any object with dense gaseous regions and a source of high-energy photons.

## 1.2 A Volume Density Experiment

This thesis will focus on abundance studies of the aforementioned emission-line compact dwarf galaxies. An emission line spectrum emanating from a dwarf galaxy is evidence of active star formation, and therefore evidence of processes of interest with regards to abundances. Classification of galaxies by metallicity, with an eye towards better understanding chemical evolution and enrichment processes, is an area of ongoing research. This thesis will conclude by characterizing a statistically complete sample of dwarf galaxies by metallicity in order to find a relationship between volume density in space and metallicity.

One of the goals of such a project is to elucidate the status of a specific object known as I Zwicky 18. The metallicity of I Zw 18 was first discovered over 30 years ago by Sargent & Searle (1970), yet it still remains the most metal-poor galaxy ever discovered in the local Universe. Numerous targeted searches, such as those described in Kunth & Sargent (1983), have been conducted attempting to locate similar objects. All these searches have failed to detect any system with lower metallicity than I Zw 18. If a volume density-metallicity relationship were known to a reasonable level of certainty it would be possible to determine whether I Zw 18 represents an absolute lower limit level of metallicity, and with what sort of volume density such metallicities occur. This would help to explain the uniqueness of I Zw 18.

In order to carry out this task, abundances must be obtained for a sufficiently large number of galaxies. In the case that it is possible to obtain a high-quality spectra (with a good signal-to-noise ratio), we may use the analytical processes described in chapters 2 and 3 to derive *nebular abundances* with very good accu-

racy. A large portion of the work in this thesis went into developing and adapting a software package to carry out this process in a consistent and efficient manner.

However, it is also sometimes the case that the spectra we obtain for star-forming dwarf galaxies do not have sufficient signal-to-noise for us to measure the flux of all the necessary lines to find nebular abundances. In this case we use what is known as the *coarse abundance* method, which involves plotting known metallicities from the nebular abundance method against the direct ratios of some lines (usually lines associated with oxygen ions) to hydrogen, and finding a fit. The resulting coefficients are then used to produce less accurate but still usable abundances given only information about a few strong oxygen and hydrogen lines.

Using data from both methods, and the spectrally-determined redshift of the galaxies to find distance and derive volume densities, it will be possible to ascertain the relationship between metallicity and volume density.

### 1.3 Reworking the Abundances Data Pipeline

Another topic that this thesis will take up is the gritty details of the process of computing nebular abundances. During the summer of 2005 I was part of a group at Williams College that began developing a new software package – intended for use with planetary nebulae located in the Milky Way Galaxy – that implemented many of the existing steps and processes involving in deriving nebular abundances. The software package was called ELSA (Emission Line Spectrum Analyzer) and had the primary goal of integrating the various steps in the abundance pipeline (the series of tasks that must be carried out sequentially to produce the final

answer) into a single, consistent piece of software that would be easily accessible to the astronomical community.

Prior to the development of ELSA, the data pipeline tended to be a quite substantial number of steps. It followed this rough outline:

1. taking data at a telescope;
2. reducing the raw data into a usable, plot-ready format;
3. measuring the strengths of emission lines that will be needed for abundance determinations;
4. correcting for reddening and galaxian stellar absorption;
5. finding the temperature and density of the object;
6. finding the abundances of specific ionization stages of elements of interest;
7. applying correction factors to account for unobserved ionization stages which are nonetheless expected to be present;
8. adding all stages together to obtain the total abundance.

A full-service software package exists to handle all aspects of steps 1 through 3: the Image Reduction and Analysis Facility (IRAF). It is well beyond the scope of this project to analyze how well IRAF does its job. Instead, we focus on steps 4 through 8 of the process.

Any astronomical observation is subject to effects that cause less light to arrive at the telescope than there ought to be based on the intrinsic brightness of the object being observed. For emission-line spectra, we must concern ourselves with

*interstellar absorption* and scattering, the wavelength-dependent removal of light from our source by dust between us and the source, and with *stellar absorption*, a process by which the hydrogen Balmer emission lines are stealthily weakened via underlying absorption lines at the same wavelengths as the Balmer emission lines. Interstellar absorption and scattering are major considerations for observing planetary nebulae and other Galactic sources. Most of them, by virtue of being former stars, reside in the Galactic disk, which is replete with dust. When observing extragalactic sources, interstellar absorption and scattering remain significant problems. Although galaxies are often located at such positions that we avoid most Galactic dust, dust in the source galaxy still weakens lines.

Additionally, a large number of stars in the host galaxy will inevitably end up in the spectrograph slit due to the low spatial resolution we have in other galaxies. This will cause the absorption-line spectrum of the stars to be superposed onto the emission line spectrum we are interested in, further complicating the process of finding the true strength of the Balmer lines. Thus, the observed strength of the Balmer lines is critical to calibrating the reddening and absorption corrections. For objects hot enough to ionize helium, recombination of free electrons with  $\text{He}^{2+}$  ions provides a spectrum of emission lines that almost exactly overlay the Balmer series, providing yet another source of contamination to be dealt with.

Once the reddening and absorption corrections are complete, we find the temperature and density. This is, in actuality, not as simple as described above. A line ratio sensitive to temperature is also sensitive (albeit less so) to density, and vice versa. We have two options: we can either always assume a constant for the less sensitive parameter and hope the real result is “close enough,” or we can de-

termine temperature and density iteratively, back and forth, until both converge on their own distinct values. The former is considerably less work, while the latter is somewhat more physically accurate.

Finally, the abundances can be calculated. The numerical calculation depends on a wealth of atomic constants, including the collision strength (i.e., the probability of excitation due to an electron-electron collision) and the probability of spontaneous de-excitation of an excited state due to bound electron interactions within the atom. These quantities are derived primarily through empirical laboratory-based experiments. They tend to be revised frequently as methods to determine them improve, so it is entirely possible for atomic data to become outdated.

Clearly, there is a series of possible snags one might hit in the process of finding nebular abundances. Hence, one of the main themes of this thesis will be to introduce ELSA as software package designed to integrate steps 4 through 8 into a unified bundle. Many data pipelines currently in use omit less essential steps to save time, involve a large amount of tedious, time-consuming manual data transfer and processing, are prone to human and/or clerical errors, or all of the above. ELSA attempts to address all of these problems. It provides a rigorous framework for the calculation of reddening/absorption corrections, temperatures, densities, and abundances. At the same time, it handles all steps internally so as to minimize intermediate data steps, thereby reducing manual labor on the part of the astronomer and the possibility for mistakes. However, ELSA is not meant to be a black box. A large amount of control over its behavior is possible through configuration options.

## 1.4 Motivation and Goals

The goals of this thesis are threefold: to demonstrate the use of ELSA to the astronomical community as a tool to carry out nebular abundance work, to use ELSA to obtain accurate nebular abundances for a previously unexplored sample of dwarf galaxies, and to undertake a study of the relationship between the chemical abundances of dwarf galaxies and their volume densities in space. In recent years, the development of astronomical software has been somewhat languid. Much of what is written is done hastily and is specific to a single astronomer's work. As such, it is never improved upon or fleshed out to the extent that it becomes a general tool for the entire astronomy community.

With the heavy dependence upon computers that the field of astronomy has developed over the past few decades, it is my belief that the importance of reliable, accurate and well-maintained software cannot be understated. I hope that this work will both shed light on an interesting and heretofore unexplored relationship within galaxy populations while also introducing what will become a valuable tool for astronomers who work in this field and demonstrating that the development of personal tools into a resource for the scientific community is a worthwhile endeavor.

# Chapter 2

## Scientific Background

### 2.1 Astrophysical Objects of Interest and the Strömgren Sphere

The emission line objects which produce the spectra under consideration in this thesis are typically gaseous regions with densities significantly greater than the ambient interstellar medium (ISM) of their host galaxy. They are located near sources of ultraviolet (UV) photons with energy  $\geq 13.6$  eV. The nature of the photon source varies for different types of objects. Planetary nebulae, comprised of the gaseous envelope shed by a star near the end of its lifetime, receive UV photons from the hot, newly-exposed white dwarf which was formerly the core of the star. H II regions, which are usually associated with a star formation event, receive their UV photons from the hot, young stars of class O or B which formed nearby. Active galactic nuclei, the central regions of galaxies with abnormally high luminosities, emit enough UV photons to produce emission lines in the gas

around them.

All the discussion in this chapter is meant to be general to all objects subject to ionization from UV photons. However, in later chapters we will take up the task of determining chemical abundances of the star forming regions of dwarf galaxies using the same physics model. To do this we must adopt the assumption that emission line dwarf galaxies are small enough that star formation events and the associated conditions dominate to the extent that the spectrum of the galaxy as a whole begins to resemble that of an H II region subject to the effects described herein.

Regardless of the energy source, the physics of these gaseous objects remains very similar. The binding energy of neutral hydrogen is  $-13.6$  eV, so the UV photons ionize the hydrogen atoms, producing the  $H^+$  ion and a large population of free electrons. Also worth noting is that neutral helium present in the gas is often ionized, producing the  $He^+$  ion which consists of a helium nucleus and a single electron – a hydrogen-like system. The ionizing photon flux spreads out, as any flux does, proportional to a  $1/r^2$  law, so there is a distinct radius beyond which there is not a sufficient number of high-energy photons to ionize hydrogen atoms. This radius defines what is known as the “Strömgren sphere.”

Within the Strömgren sphere, a large number of electrons are stripped from their host atoms by the ionizing photons. The number of free electrons becomes significant enough that electron-electron collisions (which have a relatively high cross section) become common. This in turn causes the free electron population to form a thermal Maxwell-Boltzmann energy distribution. A wealth of information may be obtained about the free electron population from the parameters of the

distribution. For example, the probability density of a specific electron speed (a useful quantity for computing collision probabilities given certain cross sections) is given by:

$$P(v) = 4\pi \left( \frac{m_e}{2\pi k T_e} \right)^{3/2} v^2 \exp \left[ \frac{-m_e v^2}{2k T_e} \right] \quad (2.1)$$

where  $m_e$  is the mass of an electron.

The only physical parameter on which this Maxwell-Boltzmann distribution depends is  $T_e$ , which is known as the *electron temperature*. It is important to note that  $T_e$  is only defined in terms of this distribution and is not necessarily the thermodynamic temperature of the gas. Another important physical parameter related to the free electron population is the number density of electrons,  $N_e$  (which has units of  $\text{cm}^{-3}$ ).  $N_e$  also affects the probabilities of various transitions and collisions. In general,  $T_e$  and  $N_e$  are understood to be functions of the physical conditions of the gas, resulting from a combination of its composition, morphology and energy source. There are specific diagnostics than may be used to find these quantities, and this will be explored further in this chapter and in chapter 3.

## 2.2 Formation of Recombination Lines

There are two types of emission lines which form through different processes within the gas. The first type is known as the *recombination lines*. These lines result from the recapture of electrons by the hydrogen and helium ions. Electrons may be recaptured to any energy level of the atom, although probability favors recapture to lower energy states. The initial recapture is a free-bound transition and may radiate a photon at any wavelength within a certain range, dependent on what

the energy of the electron prior to recombination was. In many cases the initial free-bound transition places the electron at one of the lower excited states rather than the ground state. These excited states have a very short lifetime (typically on the order of  $10^{-8}$  seconds) and almost immediately transition downward. The ensuing bound-bound transition produces a photon with a wavelength specifically corresponding to the energy difference between the two levels:

$$\lambda = \frac{hc}{\Delta E} \quad (2.2)$$

where  $\Delta E$  is the energy difference.

Bound-bound transitions to the  $n = 2$  level from any upper level form a set of lines known as the Balmer series. The lines these transitions produce are  $H\alpha$  ( $n = 3 \rightarrow n = 2$ ),  $H\beta$  ( $n = 4 \rightarrow n = 2$ ),  $H\gamma$  ( $n = 5 \rightarrow n = 2$ ),  $H\delta$  ( $n = 6 \rightarrow n = 2$ ) and  $H\epsilon$  ( $n = 7 \rightarrow n = 2$ ). Transitions from levels above  $n = 7$  are known as  $H8$ ,  $H9$  and so on. The Balmer series is of special importance to this work since all its major lines occur in the optical portion of the electromagnetic spectrum, making it an easily-observable indicator of the amount of hydrogen as well as a critical diagnostic in correcting for wavelength-dependent reddening, which will be discussed later.

Other hydrogen series exist as well. Transitions to  $n = 1$  are known as the Lyman series ( $Ly\alpha$ ,  $Ly\beta$ , ...). Transitions to  $n = 3$  form the Paschen series ( $Pa\alpha$ ,  $Pa\beta$ , ...). Transitions to  $n = 4$  form the Brackett series ( $Br\alpha$ ,  $Br\beta$ , ...). Since Lyman transitions involve greater energy differences than Balmer transitions, they radiate lines in the UV. Paschen and Brackett transitions radiate in the

infrared (IR) as they cover a smaller energy difference than Balmer lines. We will focus primarily on optical data for this work, so we use the Balmer lines as our main hydrogen diagnostic.

For recombination lines, there is still a (small) probability that the emitted photons will be absorbed by another neutral hydrogen atom, exciting its electron in turn. However, due to the typically very low electron densities of these objects (usually in the range of  $10^2$  to  $10^4$   $\text{cm}^{-3}$  – much lower than the best “vacuum” available in an Earth-based laboratory) most of the photons do not interact with another electron. Instead, they exit the gas en masse, creating an emission line. The Lyman series photons are exceptions to this, however, as there is ample neutral hydrogen in the ground state for them to interact with. They carry exactly enough energy to cause an excitation from the ground state to one of the bound excited states, so photo-ionized objects are usually optically thick at Lyman wavelengths. Balmer photons do not often encounter neutral hydrogen in the first excited state (due to the extremely short lifetime of that state), and thus they rarely are prevented from exciting the nebula.

It is also worth noting that recapture of electrons by doubly ionized helium produces a nearly parallel set of lines and series. One such series that we will contend with later is the Pickering series, which consists of transitions to  $n = 4$  in recombinant helium. The Pickering lines all radiate at wavelengths very similar to those of the Balmer series, often causing them to blend with one another in observed spectra. This is simply a consequence of Bohr’s energy equation, which gives the energy levels of a hydrogenic system (neglecting fine and hyperfine

structure perturbations):

$$E_n = -\frac{Z^2 e^4 m_e}{32\pi^2 \epsilon_0^2 \hbar^2} \frac{1}{n^2} = (-13.6 \text{ eV}) \frac{Z^2}{n^2} \quad (2.3)$$

where  $Z$  is the atomic number of the element involved,  $e$  is the fundamental charge of an electron, and  $\epsilon_0$  is the electromagnetic permittivity of free space. For helium ( $Z = 2$ ), values of  $n$  twice that of their hydrogen counterparts will clearly produce similar energies, and thus transitions to  $n = 4$  in singly ionized helium do in fact overlap the Balmer series to a significant degree.

## 2.3 Formation of Forbidden Lines

The second type of emission line results from a much more complex process known as *collisional excitation*. This is effectively observed only in atoms of the metal elements (i.e., anything heavier than hydrogen or helium) which have been partially ionized by the UV photons from the object's energy source.

Metallic ions (most commonly carbon, nitrogen, oxygen, sulfur, or heavier elements) contain multiple electrons, only a few of which have been stripped away by ionization. The quantum states of these ions are somewhat more elaborate than those of hydrogen or helium. They are normally expressed in spectroscopic notation using the electron configuration and angular momentum term. For example, the ground state of the doubly ionized oxygen ion ( $\text{O}^{2+}$ ) has six bound electrons in the configuration  $1s^2 2s^2 2p^2$  with an angular momentum term  $^3P_0$ . The angular momentum term describes the total angular momentum of the state in the form  $^{2S+1}L_J$ , where  $S$  is the spin quantum number of the system,  $L$  is the

orbital quantum number, and  $J$  is the total angular momentum quantum number. Using Hund's rules and the Pauli exclusion principle, it is possible to determine the ordering of energies of various angular momentum states which have the same electron configuration.

When a free electron makes a close approach to the ion and interacts with it, it is said that a "collision" occurs. This is true in a quantum-mechanical sense in that the wavefunctions of the free electron and the ion affect each other, although nothing necessarily "collides" in the classical sense. It is possible in this situation for a portion of the free electron's kinetic energy to be transferred to the ion, moving it into one of the excited states. The cross section for a collision which causes an excitation from a hypothetical state  $i$  to a higher-energy hypothetical state  $j$  is given by Osterbrock (2006) as:

$$\sigma_{ij}(v) = \frac{\pi \hbar^2}{m_e^2 v^2} \frac{\Omega(i, j)}{\omega_i} \quad (2.4)$$

In this equation,  $v$  is the speed of the free electron, the probability distribution of which is given by Equation (2.1).  $\omega_i$  is the *statistical weight* of state  $i$  – that is, the ratio of the number angular momentum states which produce the state's energy to the total number of angular momentum states possible in the system.  $\Omega(i, j)$  is the *collision strength*, which is uniquely defined by this equation, assuming that

$$\frac{1}{2} m_e v^2 > \chi$$

where  $\chi$  is the energy difference between the two states.  $\Omega(i, j)$  is a function of the (thermal) kinetic energy of the free electron, so in practice it is convenient

to express it as  $\Upsilon(i, j)$ , an integral of the collision strength averaged over all velocities. As given in Osterbrock, this is:

$$\Upsilon(i, j) = \int_0^\infty \Omega(i, j) \exp(-E/kT_e) d\left(\frac{E}{kT_e}\right) \quad (2.5)$$

Using this, along with Equation (2.4) and the Boltzmann equation of thermodynamic equilibrium, we arrive at  $q_{ij}$ , the number density of collisional excitations per unit time (here given in  $\text{cm}^{-3} \text{s}^{-1}$ ), as derived in Osterbrock:

$$q_{ij} = \frac{\omega_j}{\omega_i} q_{ji} \exp(-\chi/kT_e) = \frac{8.629 \times 10^{-6}}{T_e^{1/2}} \frac{\Upsilon(i, j)}{\omega_i} \exp(-\chi/kT_e) \quad (2.6)$$

The numerical value of  $\sigma_{ij}$  and by extension  $\Upsilon(i, j)$  are a matter of ongoing laboratory-based research, and are revised on a frequent basis for a host of different transitions.

The actual reconfiguration of electrons involved in a collisional excitation is not necessarily straightforward to determine, as it is with recombination processes. In many cases the excitation will involve only changing the angular momentum of an electron rather than its principal quantum number. A transition from one angular momentum state to another without a change of principal quantum number is forbidden by atomic selection rules, so such an excited state of this type is known as “metastable” since spontaneous de-excitation of it is statistically unlikely.

Because of this, metastable states tend to have very long lifetimes, compared to photonically excited states. There are two means of de-exciting them. One results from to electron-electron interactions within the ion. In this case, when the state becomes de-excited (either to a lower-energy excited state or to the ground

state) the excess energy is radiated as a photon with wavelength as defined in Equation (2.2). The probability of this radiative de-excitation is governed by a probability factor, usually known by the symbol  $A$  (sometimes called the “Einstein  $A$  coefficient”). It is generally a constant independent of temperature or density.

The other means of de-excitation is the reverse of collisional excitation, in which a free electron interacts with the ion in such a way that an amount of energy corresponding to the difference between the excited state and a lower energy state is transferred to the free electron in the form of kinetic energy. The probability of collisional de-excitation is heavily dependent on the density of free electrons, whereas radiative de-excitation is entirely independent of this.

In the density regimes observed in typical emission line objects, collisional de-excitation is vastly less probable than radiative de-excitation. Collisional de-excitation begins to dominate at a specific critical density  $N_c$ , which varies for different transitions. However, in almost all cases it is essentially impossible to create densities low enough to avoid contributions from collision de-excitation in a laboratory on Earth. Accordingly, the creation of radiative emission line spectra from multielectron ions is nigh-impossible as well. Historically, these lines have therefore been called *forbidden lines*. They are denoted by square brackets around the spectroscopic name of the ion, such as in [O III] or [S II].

Collisional de-excitation is essentially a non-factor in the objects we are interested in, which have characteristic densities of between  $10^2$  and  $10^4 \text{ cm}^{-3}$ . At these densities, practically all collisional excitations result in the formation of a photon at the wavelength of one of the forbidden lines. As the collisional excitation process reduces the kinetic speed of the free electron, it results in an overall cooling

effect on the free electron temperature. Most of the thermal energy transferred from the energy source to the gas is evacuated through this collisional excitation and forbidden line radiation process, creating a thermal equilibrium which allows most of the objects we study to remain stable.

The forbidden lines are the key to deriving metallic abundances of emission line objects. The various probabilities mentioned above are all functions only of  $T_e$  and  $N_e$ , so knowing these parameters as well as the level of hydrogen emission in the object allows solving directly for the abundances of the metal atoms.

## 2.4 Forbidden Line Sensitivity to Temperature and Density

While all the forbidden lines depend to some extent on temperature and density, some ions have lines with a very strong dependence on either temperature or density and much less dependence on the other. The lines of these ions are commonly used to obtain estimates for  $T_e$  and  $N_e$  which may subsequently be used to continue with a treatment of the actual abundances of any ion.

The lines of [O III] and [N II] are especially sensitive to  $T_e$ . This sensitivity arises from the fact that both the  $O^{2+}$  and  $N^+$  ions have six electrons and a  $2p^2$  electron configuration in their valence shell. It happens to be that such a configuration results (through various quantum mechanical effects that are beyond the scope of this thesis) in two low-lying singlet excited states ( $^1S_0$  and  $^1D_2$ ) just above the triplet  $^3P$  ground state, as described in Osterbrock (2006) and shown in Figure 2.1. In the case of [O III], the lines in question are  $\lambda 4363$ , which results

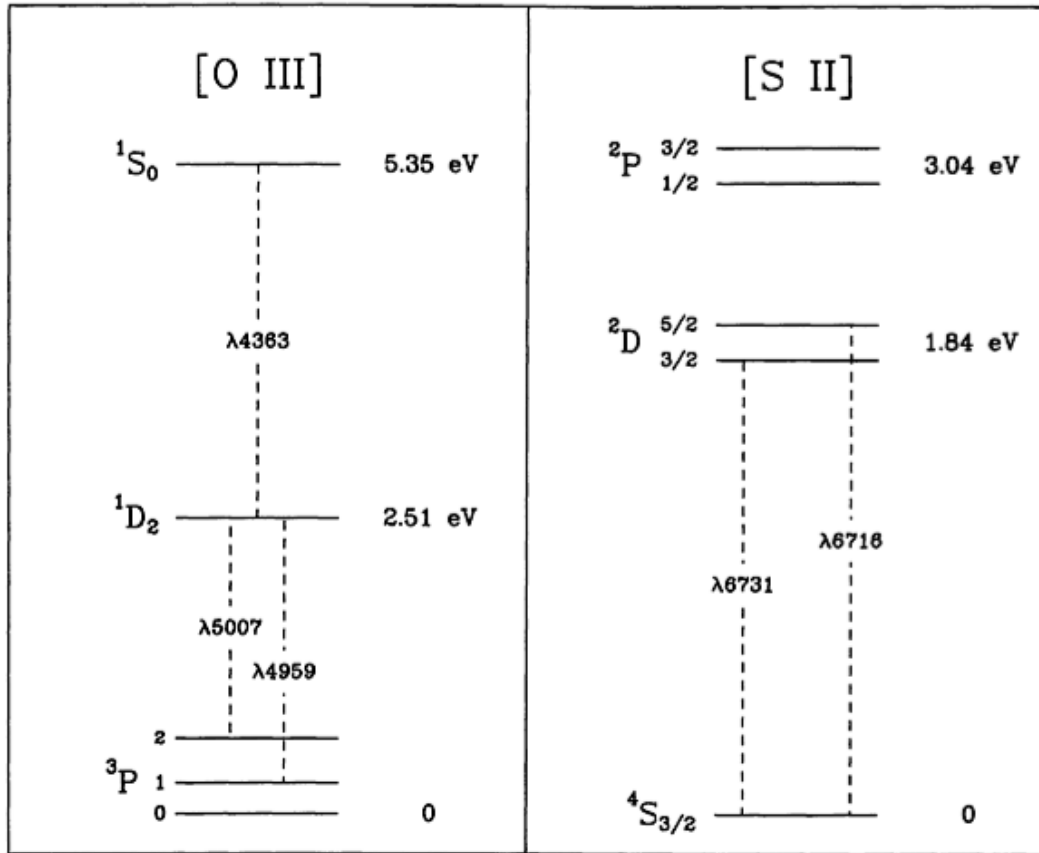


**Figure 2.1:** Energy level diagram for the  $O^{2+}$  and  $S^+$  ions. Taken from De Robertis et al. (1987)

from the  $^1S_0$  to  $^1D_2$  transition and the lines  $\lambda 5007$  and  $\lambda 4959$ , which result from the  $^1D_2$  to  $^3P_2$  and  $^1D_2$  to  $^3P_1$  transitions respectively.  $\lambda 5007$  and  $\lambda 4959$  are usually summed into a single flux as they both represent transitions to a  $^3P$  state. There is a line corresponding to the full  $^1S_0$  to  $^3P_1$  transition, which radiates at  $\lambda 2321$  (well into the UV band). The [N II] ion is fully analogous, with the  $^1S_0$  to  $^1D_2$  transition at  $\lambda 5755$  and the  $^1D_2$  to  $^3P_2$  and  $^3P_1$  transitions at  $\lambda 6583$  and  $\lambda 6548$ . The full transition is at  $\lambda 3063$ .

Collisions with free electrons may cause excitations into either of the upper

singlet levels. As discussed in the previous section, essentially all excitations will result in an emitted photon. Thus each photon from a  $^1S_0$  to  $^1D_2$  transition indicates a previous excitation from the ground state to  $^1S_0$ , and each photon from a  $^1D_2$  to  $^3P$  transition indicates an excitation from the ground state to  $^1D_2$ . According to Osterbrock (2006), population of the  $^1D_2$  level by downward radiative transitions from  $^1S_0$  may be neglected in the computation of level populations, as they are vastly outnumbered by collisional excitations from the ground state to  $^1D_2$ .

In Equation (2.6), we can see that the excitation rate increases exponentially with  $T_e$ , but the  $\chi$  factor inside the exponential will be larger for the higher energy state, creating a smaller first derivative of the function. Thus higher values of  $T_e$  will yield exponentially decreasing values of the ratio of  $j(\lambda 5007 + \lambda 4959)/j(\lambda 4363)$  (for [O III]) and  $j(\lambda 6548 + \lambda 6583)/j(\lambda 5755)$  (for [N II]) where  $j$  is the emissivity, or energy per unit volume per unit time, of the line. This is analogous to finding the ratio of (number of excitations to intermediate energy state)/(number of excitations to high energy state) over a given unit time. How this relation may be applied in practice to find  $T_e$ , and an explicit analytical solution, will be explored further in §3.4.

A very different situation applies to the  $S^+$  ion. Singly ionized sulfur has 15 electrons in the configuration  $1s^2 2s^2 2p^6 3s^2 3p^3$ . While ions with an even number of electrons (such as  $O^{2+}$  and  $N^+$ ) in the valence shell tend to produce a triplet ground state and low-lying singlet excited states, an ion such as  $S^+$ , with an odd number of electrons in the valence shell, tends to produce a quadruplet (4 times degenerate) ground state and doublet low-lying excited states. In the case of  $S^+$ ,

the ground state is the quadruplet  $^4S$ , and the excited states are  $^2D_{3/2}$ ,  $^2D_{5/2}$ ,  $^2P_{1/2}$  and  $^2P_{3/2}$  in order of increasing energy. Two transitions are useful here: the  $^2D_{5/2}$  to  $^4S_{3/2}$  transition which radiates at  $\lambda 6716$  and the  $^2D_{3/2}$  to  $^4S_{3/2}$  transition which radiates at  $\lambda 6731$ .

We will ignore the  $^2P$  states for the moment. Excitations from the ground state to either  $^2D_{3/2}$  or  $^2D_{5/2}$  require essentially the same excitation energy  $\chi$ , so the difference between their respective excitation rates as given by Equation (2.6) will be relatively invariant with  $T_e$ . The primary force controlling the ratio of ( $\lambda 6716/\lambda 6731$ ) is that of collisional de-excitation, which removes some fraction of the population of each excited state before radiation of a photon occurs.

In the low density limit where  $N_e \rightarrow 0$ , literally all excitations radiate. The exponential factor in Equation (2.6) vanishes and the ratio of photons emitted at each line depends only on the ratio of the populations of the two states (i.e., the number of excitations occurring per unit time):

$$\frac{j(\lambda 6716)}{j(\lambda 6731)} = \frac{N(^{2D_{5/2}})}{N(^{2D_{3/2}})} \propto \frac{q(^{2D_{5/2}})}{q(^{2D_{3/2}})} \quad (2.7)$$

This in turn depends on the ratio of the collision strengths and statistical weights, which is a fixed, empirical number. For the [S II] lines, it happens to be about 1.45 according to Osterbrock (2006).

In the high density limit where  $N_e \rightarrow \infty$ , collisional de-excitation dominates and must be taken into account. In this case we recall the quantities  $A_{ji}$ , the radiative de-excitation probability between state  $j$  with higher energy and state  $i$  with lower energy, and  $q_{ji}$ , the collisional de-excitation probability from  $j$  to  $i$ .

Note that while we previously considered  $q$  as the collisional excitation probability, it can represent any collisionally-induced transition, whether it be upwards or downward. In this case  $j$  is the excited  ${}^2D_{5/2}$  or  ${}^2D_{3/2}$  state and  $i$  is the ground state. Thus we have:

$$\frac{j(\lambda 6716)}{j(\lambda 6731)} = \frac{N({}^2D_{5/2})q({}^2D_{5/2}, {}^4S)}{N({}^2D_{3/2})q({}^2D_{3/2}, {}^4S)} \quad (2.8)$$

The transition between the two regimes occurs at a critical density defined by the ratio of the sum of the radiative de-excitation probabilities to the sum of the collisional de-excitation probabilities. This is the density at which the effect of collisional de-excitation becomes relevant for a given state  $i$ , given in Osterbrock (2006):

$$N_c(i) = \frac{\sum_{j < i} A_{ij}}{\sum_{j \neq i} q_{ij}} \quad (2.9)$$

The end result is that the [S II] lines show a good sensitivity over the range of densities likely to be found in astrophysical objects. For both the states discussed here,  $N_c$  is of order  $10^3 \text{ cm}^{-3}$ . The overall range of sensitivity is roughly of order  $10^2$  to  $10^4 \text{ cm}^{-3}$ . In practice, the actual value of  $\lambda 6716/\lambda 6731$  will not conform exactly to the form of either Equation (2.7) or (2.8). An analytical solution for the populations of each level is possible, but only if an assumption of a finite number of energy states is adopted. For an explicit treatment of this, see §3.4.

## 2.5 Deriving Abundances from Line Strengths

Obtaining an abundance of any given ion  $X^i$  as a ratio to the abundance of  $H^+$  is relatively straightforward given the processes and equations already described. The values of  $T_e$  and  $N_e$  must be known before any abundances are calculated. Once this has been accomplished, the equation governing the abundance is, as given in DeRobertis et al. (1987):

$$\frac{N(X^i)}{N(H^+)} = \frac{I(X^i)}{I(H\beta)} \times \frac{j(H\beta)}{j(X^i)} \quad (2.10)$$

Here  $I$  is the observed intensity (in  $\text{erg s}^{-1} \text{cm}^{-2} \text{sr}^{-1}$ ) and  $j$  is the theoretical emissivity (in  $\text{erg cm}^{-3} \text{s}^{-1}$ ). The intensity corresponds to observed data and must be corrected for absorption effects (see the following section for a brief theoretical discussion and §3.3 for an in-depth procedural treatment). The emissivities must be calculated numerically for a given line resulting from the spectrum of the ion  $X^i$ .

The emissivity for a forbidden line of ion  $X^i$  is determined quantum mechanically. The number of photons emitted per unit volume per unit time may be found given  $T_e$ ,  $N_e$ , and four atomic constants: the radiative transition probability  $A$ , the transition energy difference  $\chi$ , the collision strength  $\Upsilon$  and the statistical weight  $\omega$  corresponding to the state which radiates to produce the line in question. This calculation involves a set of equations as large as the number of states populated, so an analytical solution is only possible if one limits the number of states assumed to contain a physically significant population. Once the density of photons has been determined, the emissivity is given by simply multiplying the number by the

characteristic energy of photons at the wavelength of the line,  $E = hc/\lambda$ .

Emissivities of recombination lines rely on the so-called *effective recombination coefficient*, denoted by  $\alpha_{\text{eff}}$ . This coefficient is also simply a number of photons emitted per unit volumes per unit time. The value of  $\alpha_{\text{eff}}$  has been measured empirically, as in Storey & Hummer (1995). It is a function of both  $T_e$  and  $N_e$ . The emissivity of H $\beta$  is then given by:

$$j(\text{H}\beta) = \alpha_{\text{eff}}(hc/\lambda_{\text{H}\beta}) \quad (2.11)$$

Note that *all* abundances obtained through this method have a dependence on  $T_e$  and  $N_e$  through both the value of  $\alpha_{\text{eff}}$  and the  $T_e$  and  $N_e$  dependence of the level population of a metal ion excited state.

## 2.6 Dust and Stellar Absorption

The bane of any observational project is the inevitable removal of photons from an incoming beam of light due to absorption or scattering by dust particles along the line of sight to the object. Dust particles exist in the interstellar medium in a range of sizes. In the event that a dust particle is much larger than the wavelength range of light incident on it, it creates so-called “gray absorption,” the amount of which is constant across all wavelengths. For particles much smaller than the wavelength range, the absorption and scattering due to dust is wavelength-dependent and goes as  $\lambda^{-4}$ , in accordance with the Rayleigh scattering law. In real observations the dust effects are more closely proportional to  $\lambda^{-1}$ , indicating a range of dust grain sizes (Osterbrock, 2006). Due to the fact that smaller (bluer) wavelengths

are affected to a greater degree than larger (redder) wavelengths, absorption and scattering from dust together are often known as “reddening.”

Needless to say, a wavelength-dependent reddening effect could easily skew the results of abundance calculations significantly. By its nature the processes described in this chapter have relied heavily on ratios of various lines to indicate temperature, density and abundance. A wavelength-dependent change in the spectrum would fundamentally alter any ratio being used and thereby alter the final results.

How, then, do we correct for reddening? In the optical, the process of “dereddening” typically involves finding a known “true” value for the ratio of two Balmer lines and finding a correction factor between it and the observed value. The ratio of  $H\alpha/H\beta$  is commonly chosen since it involves the two strongest Balmer lines. Savage & Mathis (1979) developed a *reddening law* characterizing the amount of reddening due to dust which is normalized to  $H\beta$ . It is defined as:

$$f(\lambda) = 4.839 \times 10^{-14}\lambda^3 + 1.904 \times 10^{-8}\lambda^2 - 4.300 \times 10^{-4}\lambda + 1.628 \quad (2.12)$$

Note that  $f(\lambda 4861) = 0$ . All  $\lambda$  smaller than  $H\beta$  have positive values of  $f(\lambda)$ , indicating that their flux should be increased relative to  $H\beta$ , while all  $\lambda$  larger than  $H\beta$  have negative values, indicating their flux should be decreased. For a detailed discussion of the implementation of this reddening law, see §3.3.

In addition to reddening, observations of extragalactic objects often suffer from underlying stellar absorption. Usually we lack the spatial resolution necessary to avoid including in the observed spectrum a large number of stars residing in the

host galaxy. For physical reasons that are beyond the scope of this discussion, stars display an absorption-line spectrum which, for most spectral classes, includes a Balmer absorption spectrum. The background continuum in an observed extragalactic spectrum includes the emission from stars, but this emission may fall off significantly at the wavelengths of the Balmer lines. If we are observing a powerful emission line source, the effect of this underlying absorption may be completely unnoticeable at a casual glance. Fortunately, the stellar absorption may be assumed to be constant in terms of equivalent width, so it is not difficult to correct for. Further discussion of the process of correcting for this may be found in §3.3.

# Chapter 3

## The ELSA Software Package

### 3.1 Synopsis

ELSA is an integrated software package to analyze emission line data from photoionized objects which I began developing during the summer of 2005 to improve the efficiency of data processing for spectra of planetary nebulae. For this thesis, a significant amount of work went into adapting it for use with extragalactic sources (particularly in adding the ability to correct for underlying stellar absorption). The main motivation for the development of ELSA came from the fact that the typical pipeline between the measured fluxes of emission lines and the final products for a spectroscopic data set was quite arduous.

Generally, the measured fluxes had to be entered by hand into some sort of apparatus which handled the reddening correction and scaling to the flux of  $H\beta$ . All manner of jury-rigged programmatic solutions have undoubtedly been created for this purpose, many of which involve large amounts of manual data transfer,

several steps and multiple software applications. Many also bypass some fairly relevant physical effects which will be discussed later in this chapter.

The next step would be to transfer the corrected, scaled flux ratios into a specially-formatted text file to be read in by a program which computed abundances relative to hydrogen in roughly the manner described in Chapter 2. An IRAF package known as NEBULAR has been widely used for this, although many other solutions exist as well. ELSA is primarily derived from a FORTRAN program known as ABUN, originally developed by Richard Henry of the University of Oklahoma (private communication; see also Kwitter & Henry, 2001).

The final resulting abundances, along with the final scaled line intensities, would then need to be transferred and formatted by hand for inclusion into some sort of publication-quality format such as L<sup>A</sup>T<sub>E</sub>X, a popular scientific and mathematical typesetting system.

The genesis of ELSA was my attempt to reduce the amount of manual labor required by this pipeline. While it originally consisted simply of shortcuts and tools to format text and data for easy input into the next step of the process, it quickly grew to include all the major science-critical steps in the pipeline. A fundamental level of efficiency was gained by passing science data from one process to the next via data structures within a single program rather than requiring human interactions with the data to move it through the pipeline. This allows ELSA to be a clearinghouse for all the processes involved in nebular abundance analysis and make centralizing updates to data such as atomic constants and reddening laws very easy.

ELSA provides other advantages as well. It has a rigorous method of correcting

for reddening and stellar absorption, a simple and accurate error propagation scheme, and the ability to produce pre-formatted L<sup>A</sup>T<sub>E</sub>X output. In the interest of time and relevance, this chapter will focus on the scientific concepts as they are applied within ELSA and omit further detailed discussion of the procedural aspects of the program. For information on procedure and other technical details, the reader is encouraged to refer to an upcoming paper on ELSA by Johnson et al. in the *Publications of the Astronomical Society of the Pacific*.

## 3.2 Temperature and Density Calculations

As was described in chapter 2, all processes in the abundance pipeline rely heavily on electron temperature ( $T_e$ ) and density ( $N_e$ ) values to proceed. Both are key parameters in all abundance calculations. Additionally, they define the intrinsic ratio of the Balmer lines used for the reddening correction, so they are a necessary component of that process as well.

The two input parameters needed to calculate either  $T_e$  or  $N_e$  are the ratio of the flux of two emission lines which result from the same ionization stage of a specific element, and the temperature (if density is to be computed) or density (if the temperature is to be computed). It is important to note that this implies a fundamental interdependence between temperature and density, such that one can never be computed without the other. This will become important in later stages of the program.

One of the drawbacks of some codes that handle emission line spectra is that it is sometimes seen as sufficient to choose default values of either  $T_e$  or  $N_e$  to simplify

the calculation. The canonical values for photoionized objects are  $T_e = 10,000$  K and  $N_e = 100 \text{ cm}^{-3}$ . These are not bad approximations; they are actually quite close for many such objects. The final result for  $T_e$  and  $N_e$  is also much more sensitive to the observed line ratio than it is the other parameter ( $N_e$  or  $T_e$ ), which tends to be a factor in the decision to drop the dependence on the latter. If a constant value is adopted, the problem can be reduced to a single fit to empirical or theoretical data, producing a function of one variable.

ELSA's treatment of this process is somewhat more rigorous. It employs a two-dimensional cubic spline interpolation routine to recover the value of  $T_e$  or  $N_e$  that corresponds to the input parameters. For this to be possible, ELSA must have a two-dimensional table of source data relating temperature, density and line ratio incorporated into the program at compile time. The source data are generated by ELSA's five-level atom routine. It can compute the population of a given energy level (and thus the ratio of two different level populations) using the `chi5L` function described in §3.4. It is then a simple process to interpolate against these data and find the appropriate temperature or density given a line ratio and the non-variable physical parameter.

A new table of source data can be regenerated at will by the compiled version of ELSA, which can then be used to compile an updated version. This is a useful function in the event that atomic constants are updated. This changes the line ratios that specific temperatures and densities imply for any given ionization stage. A version of ELSA may then be compiled which incorporates the new constants. Finally, the tables are then regenerated, and then a fully updated version is produced using the new constants and the new tables.

Electron density in ELSA is always obtained using the [S II]  $\lambda 6716$  and  $\lambda 6731$  lines. This ratio is theoretically, and empirically, shown to be very sensitive to density (see §2.4). The electron temperature calculation uses a “multi-zone” ionization scheme. The [N II]  $\lambda 5755$  and  $\lambda 6584$  lines are used to find the electron temperature of the “low ionization” region. The [O III]  $\lambda 4363$  and  $\lambda 5007$  line ratio is used to represent the “medium ionization” region. This is due to oxygen atoms requiring a higher excitation energy to become the doubly-ionized  $O^{2+}$  ion, making the [O III] spectrum a better representation of higher temperature regions. A “high ionization” temperature using the four-times ionized [Ar V] spectrum is planned for future implementation. Similar logic applies to using [Ar V] for high ionization. Most transitions which radiate in the visible, however, can be classified as low- and medium-ionization.

One critical issue that arises in the temperature calculation is the situation in which the  $\lambda 5755$  line is not detected, which is true of almost all extragalactic sources. In this case, there is no way to compute the necessary [N II] line ratio. Pagel et al. (1992) have developed a relationship, based on models by Stasinska (1990), between the [O III] temperature and the [N II] temperature:

$$T_{e,[NII]} = 2[(T_{e,[OIII]})^{-1} + 0.8]^{-1} \quad (3.1)$$

The [O III] temperature requires  $\lambda 5007$  – usually the strongest line in any extragalactic object’s spectrum – and  $\lambda 4363$ . While it is almost impossible to detect  $\lambda 5755$  in extragalactic sources, detecting  $\lambda 4363$  is certainly possible, especially when  $T_e > 10,000$  K, since  $\lambda 4363$  is stronger at higher temperatures. Both  $\lambda 5007$

and  $\lambda 4363$  are critical for making any progress on nebular abundances of extragalactic sources.

Another issue which frequently impacts extragalactic objects is the fact that the [S II] lines are often unreliable. This may be due to the fact that they are normally fairly weak and thus usually have a poor signal-to-noise ratio for dim extragalactic objects. In some particularly unfortunate cases, the [S II] lines are redshifted into a spectral region where telluric absorption in the Earth's atmosphere causes them to become very distorted. Neither of these are usually a concern for objects located in the Milky Way. In the event that ELSA encounters an [S II] line ratio which lies outside the bounds of its interpolation tables, it aborts the attempt to find  $N_e$  with this method and adopts a default value which the user may specify prior to run time ( $100 \text{ cm}^{-3}$  is standard for H II regions).

### 3.3 Reddening and Absorption Corrections

Before obtaining any useful information from line flux data, it must be corrected for both dust absorption and scattering (a process often called “dereddening”) and for underlying stellar absorption (which only affects hydrogen and helium lines). As explained in Chapter 2, dust particles reduce flux in a wavelength-dependent manner and would cause incorrect line ratios to be used to calculate physical values. Dust could be present both in our own galaxy and (in the case of extragalactic sources) in the host galaxy.

Another environmental effect to be dealt with is that of underlying stellar absorption. This applies to extragalactic sources where the spectrograph slit

unavoidably includes a large amount of the host galaxy’s stars. The result is essentially a stellar spectrum underlying the emission line spectrum that we are interested in. When the stellar spectrum includes many hot stars (as is normal for a star-forming region), the most prominent underlying features are the Balmer absorption lines. These lie directly under the Balmer emission lines that we use to determine the amount of reddening. This proves to be problematic since the amount of absorption is, on an absolute scale, much less than the amount of emission. Thus, the “net” flux at the wavelength of the Balmer lines is an emission line, but the flux is misleadingly less than it would have been without the absorption effect.

A second type of Balmer line contamination exists in the form of the helium Pickering series. The Pickering series is the spectrum of singly ionized helium which happens to have lines all located within a few Å of the main Balmer lines wavelengths. Even at very high spectral resolution, the Pickering lines almost always blend completely with the Balmer lines. We must therefore calculate and remove the flux from these lines which results from ionized helium.

The fundamental principle of the reddening correction is that the ratio of two Balmer lines (typically  $H\alpha/H\beta$ ,  $H\gamma/H\beta$  or  $H\delta/H\beta$ ) can be known *a priori* and thus used to compute a logarithmic correction factor. For all lines, we are ultimately interested in corrected, scaled flux relative to  $H\beta$  so that we can use them as input parameters to find abundances relative to hydrogen as explained in Chapter 2. Thus the corrected flux of a line is given by the equation:

$$I(\lambda) = 100 \left( \frac{F(\lambda)}{F(H\beta)} \right) 10^{c_{H\beta}f(\lambda)} \quad (3.2)$$

where  $c_{H\beta}$  is the reddening correction factor and  $f(\lambda)$  is the so-called “reddening law” – an empirically derived-polynomial representing the wavelength dependence of the reddening effects. ELSA employs an optical reddening law developed by Savage & Mathis (1979).  $F(\lambda)$  represents the observed flux of a given line. Scaled fluxes are normalized such that  $I(H\beta) = 100$ , by convention and for readability.

The value of  $c_{H\beta}$  is determined by using the known ratio of two Balmer lines (here denoted  $a$ ). It is preferable, if possible, to use  $H\alpha/H\beta$  since  $H\alpha$  is the strongest of the Balmer lines and thus has a higher signal-to-noise ratio. Adopting  $H\alpha/H\beta$  for the purposes of example, the value of  $c_{H\beta}$  is given by the equation:

$$c_{H\beta} = \log_{10} \left( \frac{F(H\alpha)}{aF(H\beta)} \right) \frac{1}{f(H\alpha)} \quad (3.3)$$

An important (and often overlooked) physical effect is the dependence of the Balmer ratio  $a$  on the electron temperature and density of the object. ELSA has a function to compute this ratio for any given electron temperature and density. The function is based on a code called INTRAT, written and described by Storey & Hummer (1995). INTRAT uses empirical data and interpolation to recover the line ratio as a function of electron temperature and density. This method works for any hydrogenic atom. In ELSA, we have imported the data necessary to deal with hydrogen and singly ionized helium. The latter will also prove useful for the Pickering line decontamination described later.

However, finding the Balmer line ratio requires knowing the electron temperature and density. We adopt an assumption of medium ionization throughout the object for this process. Thus we must use the line ratios of [O III]  $\lambda 4363/\lambda 5007$

and [S II]  $\lambda 6716/\lambda 6731$  to find the temperature and density as described in the previous section. Unfortunately, these lines also suffer from wavelength-dependent reddening, so if we simply used the line ratio as-is from the observed data, our temperature and density would be incorrect.

So, we are faced with the paradox of needing the aforementioned line ratios to calculate  $c_{H\beta}$ , and needing  $c_{H\beta}$  to deredden the lines so we can obtain the ratios. ELSA handles this by using a series of iterations of the process to compute  $c_{H\beta}$ . It begins by adopting the assumed values of  $T_e$  and  $N_e$  mentioned above as “seed” values. This provides a workable (but somewhat less accurate) value of  $a$ , which is used to compute a “first-pass” value of  $c_{H\beta}$  using Equation (3.3). The requisite lines are then corrected using Equation (3.2) and the “correct” ratio may be obtained. ELSA then proceeds to determine  $T_e$  and  $N_e$ .

The electron temperature and density routines each require the output of one another as input. In order to obtain a reasonably accurate value for both,  $T_e$  is computed first using the seed value of  $N_e$  which the user may specify. That value of  $T_e$  is then used to find a new value of  $N_e$ , which is used to compute  $T_e$  again, and so forth. This loop proceeds until both  $T_e$  and  $N_e$  converge to within a predetermined tolerance.

Having arrived at these values of  $T_e$  and  $N_e$ , ELSA uses them to find a revised value of  $a$ , the intrinsic Balmer ratio. This is used to compute a new value of  $c_{H\beta}$  using Equation (3.2), and the entire process is repeated. This correction loop is iterated until  $a$  converges on a set value to within a predetermined tolerance. Once the final value of  $a$  is known, a new  $c_{H\beta}$  is found.

A few other processes affect this correction loop as well. In each iteration, the

Pickering line contamination must be removed from the Balmer lines before  $c_{H\beta}$  is computed for each pass. The flux of the He II  $\lambda 4686$  line is a crucial indicator of the amount of ionized helium. It results from a transition from  $n = 4$  to  $n = 3$  in an He II ion. The Pickering lines underlying H $\alpha$ , H $\beta$ , H $\gamma$  and H $\delta$  result from transitions from  $n = 6$ ,  $n = 8$ ,  $n = 10$  and  $n = 12$  (respectively) to  $n = 4$ . As previously mentioned, ELSA has a function to find the ratio of the flux of lines from any two transitions provided it knows the values of  $T_e$  and  $N_e$ . In each iteration, there is an assumed value of  $T_e$ ,  $N_e$  and  $c_{H\beta}$ . ELSA uses the former two to find the ratio of all the underlying Pickering lines to  $\lambda 4686$ , which is then dereddened using the currently assumed value of  $c_{H\beta}$ . The ratio is then multiplied by the dereddened  $\lambda 4686$  flux to find the Pickering line flux. The Balmer line in question is dereddened using the assumed  $c_{H\beta}$  and finally the Pickering line flux is subtracted from the Balmer line flux. The Balmer lines are then *re-reddened* using the inverse of Equation (3.2) and the *old* value of  $c_{H\beta}$ . A *new* value of  $c_{H\beta}$  is then immediately calculated using Equation (3.3), and the loop continues normally. If  $\lambda 4686$  is not detected in the spectrum, all helium contamination corrections are bypassed. Helium contamination is mostly an issue in denser objects such as planetary nebulae. While it is possible in extragalactic sources, it is very rare.

The final correction ELSA makes is for underlying stellar absorption, which affects only extragalactic objects. The methodology for stellar absorption is to assume a wavelength-independent level of absorption in terms of equivalent width (in Å) for all Balmer lines. In order to convert line strengths from flux units to equivalent width, a measurement of the continuum flux level is required. The

equivalent width is given by

$$W = \frac{F_{\text{line}}}{F_{\text{cont}}} \quad (3.4)$$

where the units of  $F_{\text{line}}$  are  $\text{erg s}^{-1} \text{cm}^{-2}$  and the units of  $F_{\text{cont}}$  are  $\text{erg s}^{-1} \text{cm}^{-2} \text{\AA}^{-1}$ , so the units of  $W$  are  $\text{\AA}$ .

In the first iteration of the main correction loop, the helium-decontaminated Balmer lines are converted to equivalent widths. A table is generated of the  $c_{\text{H}\beta}$  value for all three Balmer line ratios ( $\text{H}\alpha/\text{H}\beta$ ,  $\text{H}\gamma/\text{H}\beta$  and  $\text{H}\delta/\text{H}\beta$ ) at varying assumed levels of absorption. The default range is  $0.0 \text{\AA}$  to  $5.0 \text{\AA}$  with a step size of  $0.5 \text{\AA}$ , although these values are easily configurable. Error bars are computed for each entry in the table to allow quantitative comparisons. The user is then prompted to enter what appears to be the correct level of absorption, which is ideally where the  $c_{\text{H}\beta}$  values for all three Balmer ratios match to within the error bars.

Due to the interactivity of this process, it is only run once in the first iteration of the loop. Since absorption is independent of all other processes that affect the reddening correction, the first-pass answer for the amount of absorption continues to be reliable for the rest of the loop. The appropriate level of absorption is converted back into integrated line flux using Equation (3.4) and added to the Balmer lines. Values of  $c_{\text{H}\beta}$  are computed for each of  $\text{H}\alpha$ ,  $\text{H}\gamma$  and  $\text{H}\delta$ , and a weighted mean value of  $c_{\text{H}\beta}$  is obtained. The dereddening loop then continues normally until convergence of the value of the intrinsic Balmer ratio. Once the loop ends, the final value of  $c_{\text{H}\beta}$  is used in Equation (3.2) to find the corrected and scaled flux for each line.

The user may specify what the final output product from a run of ELSA should

be. If the preferred product is a table of corrected line strengths relative to  $H\beta$ , the program reads a list of lines of interest specified by the user and searches for each line in the input spectrum. Upon finding it, the line's raw flux (as measured by IRAF) is corrected for reddening using the final value of  $c_{H\beta}$  and computed as a fraction of  $H\beta$  (where  $F(H\beta) = 100$ ).

If the user requested abundances as the final output product, the reddening correction process described here runs, but the resulting line fluxes are passed as a data structure to the abundance routines rather than being handled as the final output.

### 3.4 Abundance Calculations

Abundance calculations are the next logical step in ELSA once corrected line fluxes relative to  $H\beta$  are computed. As explained in chapter 2, we can only obtain abundances of various metal ions relative to the  $H^+$  ion, which is the rationale for normalizing all fluxes to that of  $H\beta$  after the dereddening process. All these data are passed to the abundance routines within a data structure as part of normal program flow. No user interaction is needed to move the data from the reddening correction stage to the abundance calculation stage.

The treatment of the level populations and abundances in §2.5 is the general case, in which any energy levels are theoretically permissible. For computational expediency, ELSA adopts what is known as the “five-level atom approximation.” The analytical solution of the abundance equations for a five-level atom was developed by Aller (see his 1984 review) and implemented in code by DeRobertis

et al. (1987). This approximation permits only the first five energy levels to be populated and assumes the population of all other levels is negligible.

Equation (3.2) gives the quantity  $I(\lambda)$ , the flux scaled relative to  $H\beta$ . This is exactly equivalent to the first factor on the right-hand side of Equation (2.10) – the ratio of the observed flux of the line of interest to the observed flux of  $H\beta$ . Prior to running any abundance calculations, ELSA computes the values of  $T_e$ ,  $N_e$  and  $\alpha_{\text{eff}}$  (the effective recombination rate for hydrogen). The former two are computed in the manner described in the previous section. The latter, as a function of  $T_e$  and  $N_e$ , is calculated using a fit to data from Storey & Hummer (1995). The number of photons  $x_i$  emanating from the transition of interest is calculated using ELSA’s `chi5L` function, which is derived in large part from Richard Henry’s `ABUN` code (received via private communication). The name of this function is a consequence of its historical development and should not be confused with  $\chi$  – the energy difference for a transition of interest – as used in this thesis.

The `chi5L` function assumes a system of five energy levels, corresponding to the ground state and the first four excited states of the system. First, a line is selected to represent the ion being processed. Only one line is necessary, so normally the line expected to be the strongest is chosen so as to maximize signal-to-noise. In some cases where discrepancies are expected between the abundance results from different lines of the same ion, a calculation is performed using multiple lines. ELSA then calculates a weighted mean using the error bars of all the outputs to produce a “best estimate” output.

The function takes as input, in addition to  $I(\lambda)$ , the previously computed  $T_e$  and  $N_e$  as well as the atomic constants  $\chi$ ,  $A$ ,  $\Upsilon$  and  $\omega$  (as discussed in the

previous chapter) for all five levels of the ion in question. Depending on which ion is being considered, the low ionization or medium ionization value of  $T_e$  will be passed to `chi5L`. All atomic constants are contained in header files in the source code, so they are included in the ELSA program at compile time. ELSA also includes auxiliary tools to update its header files to the latest versions of the atomic constants via the Internet. The primary mechanism for this is a Python script which interacts with TIPBase, the web-based data repository of The Iron Project (an ongoing research effort to catalogue atomic data with astrophysical significance). The script retrieves the most recent versions of the constants used in ELSA and automatically inserts them into source code header files. Citations for each piece of data are tracked and reported in a text file which the user may refer to if necessary.

The analytical solution of the system contains five unknowns (the populations of the five energy levels) and can be expressed as five equations. The `chi5L` function thus solves a 5x5 matrix equation in the form  $\mathbf{Ax} = \mathbf{b}$  and obtains the column vector  $\mathbf{x}$ , which represents the number density of excitations to each level. The matrix equation is:

$$\begin{pmatrix} 1 & W_{12} & W_{13} & W_{14} & W_{15} \\ 1 & W_{22} & W_{23} & W_{24} & W_{25} \\ 1 & W_{32} & W_{33} & W_{34} & W_{35} \\ 1 & W_{42} & W_{43} & W_{44} & W_{45} \\ 1 & W_{52} & W_{53} & W_{54} & W_{55} \end{pmatrix} \begin{pmatrix} x_1 \\ x_2 \\ x_3 \\ x_4 \\ x_5 \end{pmatrix} = \begin{pmatrix} 1 \\ 0 \\ 0 \\ 0 \\ 0 \end{pmatrix} \quad (3.5)$$

The non-unity matrix elements  $W_{ij}$  have the form:

$$W_{ij} = \begin{cases} \frac{C\Upsilon(i, j)}{\omega_i} e^{-\chi_{ji}/kT_e} & i < j \\ -\sum_{k=1}^{i-1} A_{ik} - \frac{C}{\omega_i} \left( \sum_{k=1}^{i-1} \Upsilon(k, i) + \sum_{k=i+1}^5 \Upsilon(i, k) e^{-\chi_{ki}/kT_e} \right) & i = j \\ A_{ij} + \frac{C\Upsilon(j, i)}{\omega_i} & i > j \end{cases}$$

where  $C$  is a constant defined in terms of the electron temperature and density such that

$$C = (8.629 \times 10^{-6} \text{ cm}^3 \text{ K}^{1/2}) \frac{N_e}{\sqrt{T_e}}$$

which may be derived from Equation (2.6).

The matrix elements incorporate both the probabilities of upward excitations via collisions (via the  $\Upsilon$  terms) and downward transitions resulting photon emissions via the transition probabilities (the  $A$  terms).

Once the solution to Equation (3.5) has been obtained, the level of interest  $x_i$  is then selected from the resulting column vector and multiplied by the photon energy associated with the wavelength of the selected line. The quantity  $j(\text{H}\beta)$  is computed using Equation (2.11). The final abundance is then computed using Equation (2.10) as all quantities involved are now known.

The total abundance of the metal elements is found by taking the sum of all ionization stages for which abundances can be calculated given the observed data. In some cases the lack of data outside the optical prevents us from obtaining any

information about some ionization stages. In these instances *ionization correction factors* (ICFs) are applied to compensate for unobserved ionization stages when finding total elemental abundances. An ICF consists of a number  $\geq 1$  by which the observed total abundance is multiplied to obtain the “true” abundance. The ICF calculations in ELSA have all been collected from the literature for various elements.

Of particular note is the oxygen abundance, for which the ICF is always given as 1. This is due to the fact that only the first and second ionization stages of oxygen ( $O^+$  and  $O^{2+}$ ) occur with any frequency in photo-ionized objects. Fortunately, all the major emission lines of these ions radiate in the optical. As an example of a non-unity ICF, the nitrogen ICF is given by Izotov et al. (1994) and is defined as:

$$\text{ICF(N)} = \frac{(O/H)}{(O^+/H^+)} \quad (3.6)$$

in which oxygen abundance is used as roughly analogous to nitrogen abundance. Since we observe both the [O II] and [O III] ions for oxygen, this formula corrects for the unobserved [N III] spectrum which is assumed to be significant to nitrogen. Most ICFs are a by-product of using only optical data to obtain abundances. In some cases the abundances of additional ionization stages (e.g.,  $S^{2+}$ ) can be known empirically if ultraviolet or infrared spectral data is available.

ELSA has a number of other features which are somewhat beyond scope of this project, but which are worth a brief mention. The helium elemental abundance is computed using recombination lines (such as  $\lambda 4686$ ) and empirical values of  $\alpha_{\text{eff}}$  for helium. This empirical data is taken from Storey & Hummer (1995). ELSA includes support for several ionization stages of a variety of elements. Although

we will only discuss oxygen, nitrogen and sulfur in this work, ELSA can find abundances for (in addition to helium): argon, carbon, chlorine and neon.

### 3.5 Error Propagation

ELSA can calculate the formal error for all output quantities, including corrected and scaled line fluxes, temperatures, densities, ionic abundances and elemental abundances. This step is entirely optional and requires a formal error for all input values (raw line fluxes). This capability represents a significant improvement over most abundance codes, in which the formal errors are ignored entirely or estimated using less rigorous methods. It should be noted if error calculation is disabled by the user, some other processes will be affected. Weighted means default to plain arithmetic means and the error bars used in the  $c_{H\beta}$  comparisons for underlying stellar absorption rely only on the assumed error of the absorption, not on both the absorption error and the flux error (the latter of which is typically much more significant).

The error bar determination in ELSA relies strictly on the formal statistical error propagation Equation:

$$\sigma_f^2 = \left(\frac{\partial f}{\partial x}\right)^2 \sigma_x^2 + \left(\frac{\partial f}{\partial y}\right)^2 \sigma_y^2 + \dots \quad (3.7)$$

where  $\sigma_f$  represents the formal error in a hypothetical function  $f = f(x, y, \dots)$  and  $\sigma_x, \sigma_y, \dots$  represent the formal errors in that function's input parameters.

In theory, each output value in ELSA is a function of as many input parameters as there exist lines in the input spectrum. This means that the above equation –

an instance of which exists for all output values, be they line fluxes or abundances – contains a term for all input lines. The formal errors for the input values ( $\sigma_x, \sigma_y, \dots$ ) are known *a priori*. The user may choose to input them explicitly or instruct ELSA to determine them automatically. If the latter is chosen, ELSA assumes an error of  $\pm 10\%$ ,  $\pm 30\%$ ,  $\pm 50\%$  or  $\pm 100\%$  as indicated by flags set by the user in the input files, or an error of  $\pm 10\%$  at all times if no flags were set. Assuming a uniform percentage error for all lines is not recommended. The most rigorous method of deriving the formal input errors is to recover them based on the response function of the spectrograph with which the data were originally taken.

As the  $\sigma$  factors in the error propagation equation are known, ELSA must then calculate the partial derivative factors. This is done in an entirely numerical fashion – the complexity of the equations involved in the dereddening and abundance phases of the program makes them evaluating them analytically a difficult process, and the numerical method is equally valid. Therefore, numerical differentiation is used to obtain all partial derivatives. For each output parameter  $f$ , the program steps through all input parameters  $x$  and varies them by their formal error multiplied by a factor that decays exponentially with each iteration of the loop. The resulting step in the value of  $f$  is determined, and ELSA calculates the quantity  $\Delta f / \Delta x$ , iteratively, until convergence is achieved for *all* partial derivatives for each output. This is the numerical equivalent of taking the limit as  $\Delta x \rightarrow 0$ . In the event that convergence does not occur, the loop ends after a fixed number of iterations (default 20, but configurable by the user) and averages the final two values to use as the result of the partial derivative.

It should be noted that most of the partial derivatives for any output will evaluate to 0 on the first iteration. For example, if the input flux of an argon line affects *only* the argon abundance outputs, the partial derivatives for all other elements' abundances with respect to that argon line will evaluate to 0. Some lines, however, affect all outputs. The [O III]  $\lambda 4363$  and  $\lambda 5007$  lines are used to compute the electron temperature used in the dereddening correction. All lines are dereddened using this factor, so the partial derivative of all outputs with respect to these lines will likely evaluate to non-zero. Thus, while it may seem like a daunting number of partial derivatives must be calculated, only a finite number of them for each output will actually prove to be relevant.

Nonetheless, it is true that enabling the error propagation functions in ELSA adds significant computation time to any given task. For example, instead of running the abundance calculation once using only the nominal values of all inputs, it must be run at least twice – and quite possibly more than twice – for *each* unique combination of inputs and outputs. While the single run is nearly instantaneous, a full run with error propagation may take several minutes for an object with a large number of lines. Using fewer lines, and running ELSA on a computer with a very fast processor, will decrease the run time significantly.

Once all partial derivatives have been computed, the final formal error for each output is determined and output alongside the nominal values in the final product.

There are a few other miscellaneous uses of error estimates in ELSA. As mentioned in §3.4, some ionic abundance calculations tend to differ based on which line's flux is used to represent the population of an ion. This is mostly due to

uncertainties and noise in the process of finding the final fluxes. In order to find the appropriate mean of two or more answers for an abundance, ELSA computes a *weighted mean* which takes into account the uncertainty in the various answers. For a quantity  $x$  where the mean  $\bar{x}$  is computed using a series of  $n$  measurements  $x_i$  with corresponding uncertainties  $\sigma_i$ , the value of  $\bar{x}$  is:

$$\bar{x} = \frac{\sum_{i=1}^n x_i / \sigma_i^2}{\sum_{i=1}^n 1 / \sigma_i^2} \quad (3.8)$$

and the uncertainty  $\sigma_{\bar{x}}$  is:

$$\sigma_{\bar{x}}^2 = \frac{1}{\sum_{i=1}^n 1 / \sigma_i^2} \quad (3.9)$$

Finally, the error bars used in the  $c_{\text{H}\beta}$  comparison for underlying stellar absorption described in §3.3 are computed by manipulating Equations (3.3) and (3.7) into the specific form:

$$\sigma_c^2 = \left( \frac{\sigma_{F(\lambda)}}{F(\lambda)} \cdot \frac{1}{f(\lambda) \ln(10)} \right)^2 + \left( \frac{\sigma_{F(\text{H}\beta)}}{F(\text{H}\beta)} \cdot \frac{1}{f(\text{H}\beta) \ln(10)} \right)^2 \quad (3.10)$$

where  $\lambda$  represents the wavelength of either H $\alpha$ , H $\gamma$  or H $\delta$ ,  $F$  represents the flux, and  $f$  represents the reddening law. The uncertainty  $\sigma_{F(\lambda)}$  (including for H $\beta$ ) is actually given by:

$$\sigma_{F(\lambda)} = \sqrt{\delta F(\lambda)^2 + \delta F_{\text{abs}}^2} \quad (3.11)$$

where  $\delta F_{\text{abs}}$  is the assumed uncertainty in the flux added to the observed line strength to correct for underlying absorption. This quantity is varied for each

absorption step to produce the table of  $c_{H\beta}$  values. ELSA currently takes this uncertainty to be 10% of the added flux. In the event that the user disables error propagation,  $\delta F(\lambda)$  is taken to be 0, so the error bars will only depend on assumed absorption flux uncertainty.

### 3.6 Limitations of ELSA

While ELSA does provide a high level of accuracy and efficiency in its processing of emission line data, there are several key limitations to it. The most significant of these is that it is strictly dependent on the presence of the Balmer lines to function correctly. If the  $H\beta$  line is not detected in the input spectrum, ELSA returns an error and exits. This also occurs in the absence of the other Balmer line chosen by the user to form the ratio used for dereddening (the default is  $H\alpha$  although  $H\gamma$  and  $H\delta$  may be selected as well).

This dependence on the Balmer series means ELSA requires optical band data to produce any results. Preliminary support currently exists to handle infrared (IR) and ultraviolet (UV) data. Reddening laws exist for this data in addition to the Savage & Mathis (1979) law for optical data. For UV, a law from Seaton (1979) is used. For IR, laws from Indebetouw et al. (2005) and Rieke & Lebofsky (1985) are implemented. It is important to note, however, that UV and IR data must also be accompanied by an optical spectrum of the same object. ELSA will normalize the IR or UV data to the scale of the optical data and calculate a value of  $c_{H\beta}$  using the Balmer lines, then use the appropriate  $f(\lambda)$  to correct the IR or UV data.

ELSA has methods to determine  $N_e$  using IR lines, but they have been tested much less and are not as robust as using the [S II] optical lines to find the density.

# Chapter 4

## Nebular Abundances of KISS Dwarf Galaxies

### 4.1 Objectives

The goal of the remainder of this thesis will be to employ ELSA to obtain nebular abundances of a new set of spectroscopic data. These data are useful in their own right, as it adds to the existing repository of nebular abundances for emission-line dwarf galaxies. Furthermore, using ELSA to obtain these abundances provides a means to validate it as a tool for abundance work since its results may be compared to previously published results to ensure the answers are reasonable and believable. Discussions of variations and discrepancies between ELSA and existing results will follow. The nebular abundances calculated in this chapter will also become part of a larger set of abundance data which will be used to establish a relationship between the volume density of galaxies and their metallicity.

As described in previous chapters, the presence of specific emission lines is required to obtain a meaningful measurement of certain physical quantities in photo-ionized objects such as the dwarf galaxies which will be discussed in this chapter. For this reason, oxygen temperatures and abundances are heavily favored for optical observations due to the fact that the two major ionization stages of oxygen present in photo-ionized objects ( $O^+$  and  $O^{2+}$ ) both produce lines which happen to radiate in the optical:  $\lambda\lambda 3726/3729, 7325$  for  $O^+$  and  $\lambda\lambda 4363, 4959/5007$  for  $O^{2+}$ . The elemental abundance  $O/H$  is typically the indicator of choice for general metallicity of photo-ionized objects, since it can be derived entirely from the ionic abundances of  $O^+$  and  $O^{2+}$ . As a further benefit, no ionization correction factor is needed since no major ionization stages of oxygen are unobserved, even when only optical data are available.

In order for nebular abundances to be calculated using the methodology described in §3.4, we must find a temperature as described in §2.4. The [O III] temperature is especially critical to finding many abundance quantities. It is also important to note that, particularly in the context of ELSA, the [O III] is also used to derive an estimate for the low-ionization region temperature (see §3.2) in the event that the [N II]  $\lambda 5755$  line is not available. Finding the [O III] temperature requires the presence of the strong [O III]  $\lambda\lambda 4969/5007$  lines as well as the weak [O III]  $\lambda 4363$  line. Spectra in which this set of lines is available are known as *abundance quality*, in that they may be used to find nebular abundances. This is not to say that other spectra are not worth obtaining. However, abundances from these spectra can only be found indirectly using relationships originally derived from nebular abundances. These relationships are known as the *strong line*

method and the *coarse abundance* method. While often quite useful in an aggregate sense, abundances obtained through this process are not as accurate as true nebular abundances.

In this chapter, we present new nebular abundances for a set of 12 galaxies which have not previously been included in an abundance study. Discussion follows of the survey from which the galaxies were selected, the criteria for selecting them, the observing parameters, and the data reductions. These abundances will also become part of a larger stock of nebular abundances which will be used in statistical studies such as the one carried out in Chapter 5. They are also instrumental in calibrating the aforementioned strong line and coarse abundance methods.

## 4.2 Candidate Galaxy Selection Criteria

Our sample is drawn from the KPNO International Spectroscopic Survey (KISS), first described in Salzer et al. (2000). The goal of KISS was to identify active emission-line galaxies (i.e., AGNs or star-forming galaxies) in the nearby Universe and to obtain positions, magnitudes, colors and redshifts for them. The survey was carried out using the wide-field Burrell-Schmidt telescope at Kitt Peak National Observatory, with a large CCD detector and an objective prism as a disperser element. This produced low-resolution spectra of thousands of objects per exposure, yielding typically between 20 to 30 objects per field which were found to be emission-line galaxies. Two separate surveys were conducted: red and blue. The red survey used a filter designed to isolate the  $H\alpha$   $\lambda 6563$  line in the

objective-prism spectra to redshifts up to  $z = 0.095$ , and selected galaxies which showed visible emission in that line. The blue survey used similar methodology to select galaxies using the [O III]  $\lambda 5007$  line.

The location of the emission line was used to obtain an estimate of the galaxy's redshift. All objects were also observed in direct imaging mode in addition to objective-prism mode in order to obtain accurate positions as well as standard  $B$  and  $V$  magnitudes. KISS is capable of detecting most line-emitting galaxies to about  $B = 19$  or  $20$  on the standard magnitude scale, and detects strong-lined objects as faint as  $B = 22$ . It is statistically complete to a certain line flux level (known as the *completeness limit*) in both surveys – that is, the survey detected *all* existent objects within the redshift limit whose  $H\alpha$  or [O III]  $\lambda 5007$  line flux was above the completeness limit. KISS is the deepest, objective-prism survey carried out to date. It also provides an excellent basis for selecting candidates for followup nebular and coarse abundance studies. This usually entails obtaining observing time for a conventional spectroscopic study and observing a subset of KISS galaxies thought to be of interest. The statistical completeness of KISS is also an important consideration in deriving a metallicity-volume density relationship.

As of this writing, a significant amount of follow-up work has already been performed on the KISS catalog, although there still remains a large body of objects whose spectral characteristics have never been explored beyond their initial observation. In particular, a large database of follow-up spectra exists with sufficient line detections to use the coarse method to obtain abundances. In the next chapter, we will take up the task of using the coarse abundance method to generate a large enough set of data points to proceed with the volume density

experiment. However, the goal of this chapter is to add to the database of direct nebular abundances obtained using the electron temperature.

For the nebular abundances, our data pool consists of galaxies selected from the KISS red and blue surveys. We selected galaxies based on the likelihood of observing the  $\lambda 4363$  line. While the  $\lambda 5007$  line is essentially always observable in dwarf galaxies, the auroral  $\lambda 4363$  is significantly more elusive. Despite this, the [O III] spectrum is still the most available and most reliable method for finding an electron temperature. In theory we would also like to find a low-ionization temperature using [N II] lines, but the undetectability of  $\lambda 5575$  in almost all dwarf galaxies makes this impossible, and we must rely on the “fallback” mechanism for finding low-ionization temperature using the medium-ionization [O III] temperature as described in §3.2. For this reason, the detectability of  $\lambda 4363$  is the lynchpin of whether the spectrum will be abundance quality, and so we used it as the primary selection criteria. A secondary effect of this selection criteria is that the galaxies we chose were likelier to be both low in abundance and in luminosity. For a discussion for why this tends to be the case, see Melbourne & Salzer (2002).

For some KISS galaxies, a “quick look” spectrum had previously been taken using a short exposure time as part of a general inventory of the catalog. These spectra themselves are too low in signal-to-noise to be abundance quality, but they are crucial in determining whether a longer investment of observing time is warranted (i.e., if  $\lambda 4363$  appears in the spectrum). Where possible, we relied on this to guide our decisions about which candidates to observe. The other means of estimating whether  $\lambda 4363$  could be detected involves using only the strength of

the objective-prism emission line from the original KISS images. In this, we adopt the assumption that high intensity of either the  $\lambda 5007$  or  $H\alpha$  suggests the signal-to-noise ratio of the galaxy spectrum is high enough that  $\lambda 4363$  is detectable.

### 4.3 Data Reductions and Processing

Data for all candidate galaxies were obtained at Lick Observatory using the 3 m telescope over the course of two observing runs in 2004 and 2005. Observations covered the entire range of the optical band using a dichroic beam splitter to pass light from the red and blue ends of the spectrum to different disperser elements. Total spectral coverage was 3500 Å to 7800 Å with a spectral resolution of 2.32 Å pixel<sup>-1</sup> for the red side and 1.85 Å pixel<sup>-1</sup> for the blue side. All targets were assumed to be capable of providing abundance-quality spectra, and were thus afforded 80 minutes of observing time each in order to obtain a high signal-to-noise ratio. All observations were accompanied by the usual complement of Hg-Cd-Ne and Ne-Ar lamp spectra (for wavelength calibration) and standard star spectra (for flux calibration).

Initial processing was done using the Image Reduction and Analysis Facility (IRAF). All instrumental bias levels were calculated and removed from each spectrum on site by the telescope's image acquisition software. In later processing, any two-dimensional structure was removed using a combined bias frame taken during the observing runs. Routine flat fielding (using quartz lamps as a uniform illuminator) was done to correct for CCD sensitivity variations. The APALL task within IRAF was used to extract one-dimensional spectra. Extraction widths were

determined by inspection for each object. A sky spectrum was obtained from the area outside the object window and subtracted from each object spectrum. The wavelength scale was calibrated using the lamp spectra, and the flux scale was established using standard star observations. The standard star spectra were also used to correct for telluric absorption in the Earth's atmosphere. In some cases, the [S II]  $\lambda\lambda 6716, 6731$  lines (which are used to find electron density) are redshifted into spectral regions of strong telluric absorption (e.g., the  $B$  band at  $6850 \text{ \AA}$ ). Failing to correct for this would make density measurements entirely unreliable. Examples of fully reduced spectra are shown in Figure 4.1.

The actual integrated flux and continuum level for the relevant emission lines in each spectra were measured using the `SPLIT` task in IRAF. The formal error in the integrated flux of all the lines is an important input for ELSA, so these were recovered using the uncorrected count rate from the extracted spectrum to determine the Poisson noise. Formal errors were then calculated using the detector's response function determined by IRAF. As the dichroic element on the telescope splits the spectra into essentially two separate observations, it was also necessary to ensure that the flux scaling was consistent between the red and blue ends of the spectrum. There is a small overlap region, ranging from roughly  $5000 \text{ \AA}$  to  $5800 \text{ \AA}$ . The continuum flux in this region was used to determine a scaling factor between the red and blue ends of the spectrum. This step is quite critical, since  $H\alpha$  and  $H\beta$  always fall on opposite segments of the spectrum, meaning that an inconsistent flux scale would severely compromise the reddening correction described in §3.3.

Once integrated line fluxes and their formal errors were measured, ELSA's

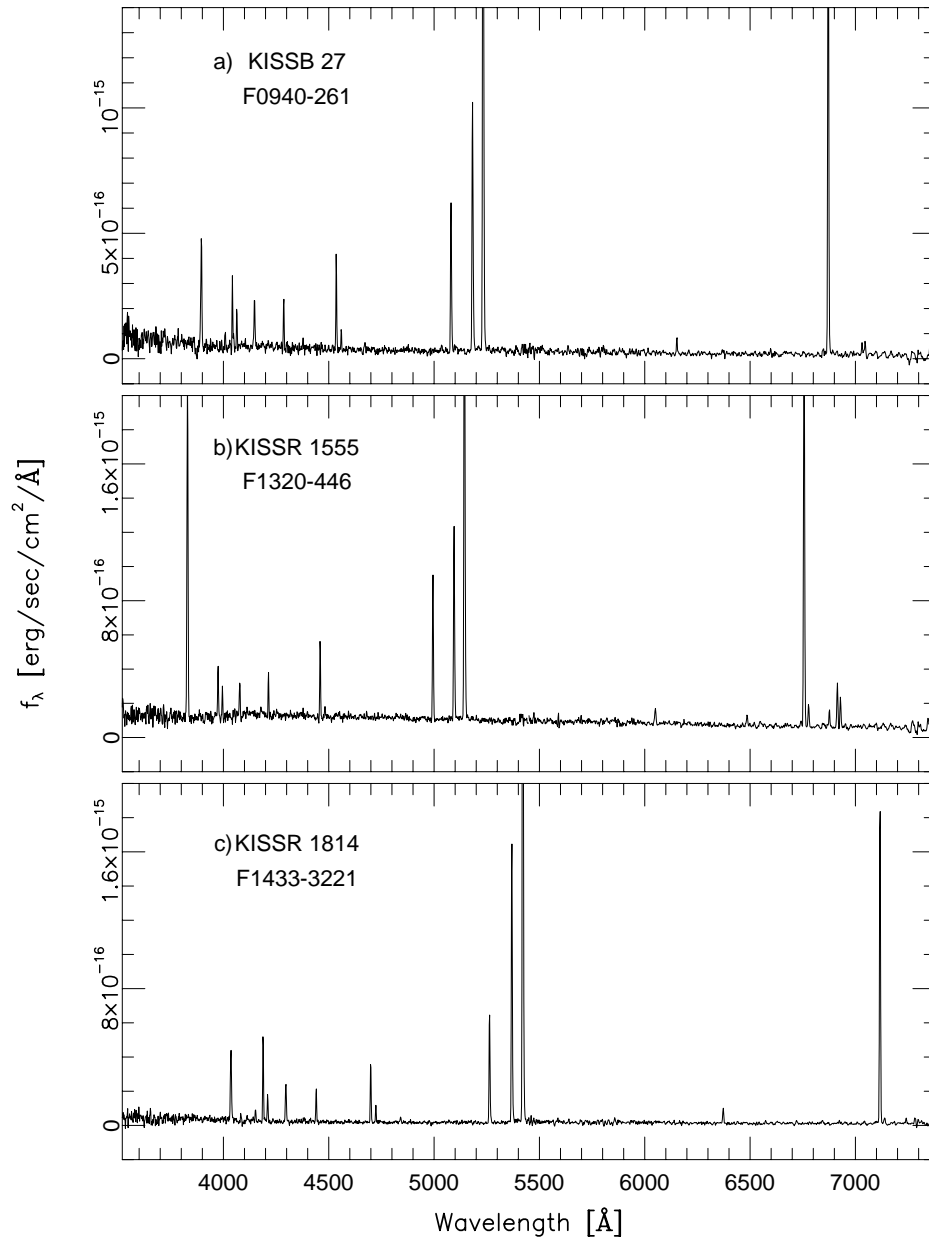


**Figure 4.1:** Reduced spectra for three KISS dwarf galaxies.

SLOT\_ABUN task was used to compute nebular abundances using the processes described in detail in §3.2-4. This task requires as input the recessional velocity of the object, usually denoted  $cz$  (as the redshift  $z$  denotes the fraction of the speed of light with which the object is receding). A value for  $cz$  was obtained, once lines in the spectrum were identified, by comparing known rest wavelengths to the observed wavelengths. For extragalactic sources such as these dwarf galaxies, ELSA also requires the user to input an estimate for the amount of underlying Balmer absorption (see §3.3). These determinations were made by inspection of the test grid of  $c_{H\beta}$  values and are included in Table 4.1.

## 4.4 Nebular Abundances From ELSA

Nebular abundances were derived for 12 KISS dwarf galaxies selected for  $\lambda 4363$  detectability. Six targets are from the red survey and six are from the blue survey. What follows are tables of scaled, corrected line intensities normalized to  $H\beta$  for the relevant emission lines in this study along with the final weighted mean values of  $c_{H\beta}$  and the amount of underlying stellar absorption used to correct the Balmer lines. The  $\log F(H\beta)$  parameter gives the logarithm of the corrected flux of  $H\beta$  in  $\text{erg s}^{-1} \text{cm}^{-2}$ . Also included are tables of the nebular ionic and elemental abundances, along with electron temperatures and densities. All figures were obtained with ELSA's SLOT\_TABLE and SLOT\_ABUN tasks using output from IRAF's SLOT task. Objects denoted with **KB** are from the KISS blue survey, while objects denoted with **KR** are from the KISS red survey.

The diagnostic diagram, which plots the quantities  $\log ([\text{OIII}] \lambda 5007 / H\beta)$  vs.

$\log([\text{NII}] \lambda 6583/\text{H}\alpha)$ , is shown in Figure 4.2 and was derived using the corrected flux of the aforementioned lines. Star-forming galaxies can be identified using the diagnostic diagram, since they all fall on the characteristic curve shown in Figure 4.2. The galaxies in this study tend to fall on the upper end of the plot. This is the result of being selected for  $[\text{O III}] \lambda 4363$  detectability. Strong  $\lambda 4363$  lines are associated with low abundance, which is in turn associated with a larger  $[\text{O III}] \lambda 5007$  flux (relative to other lines).

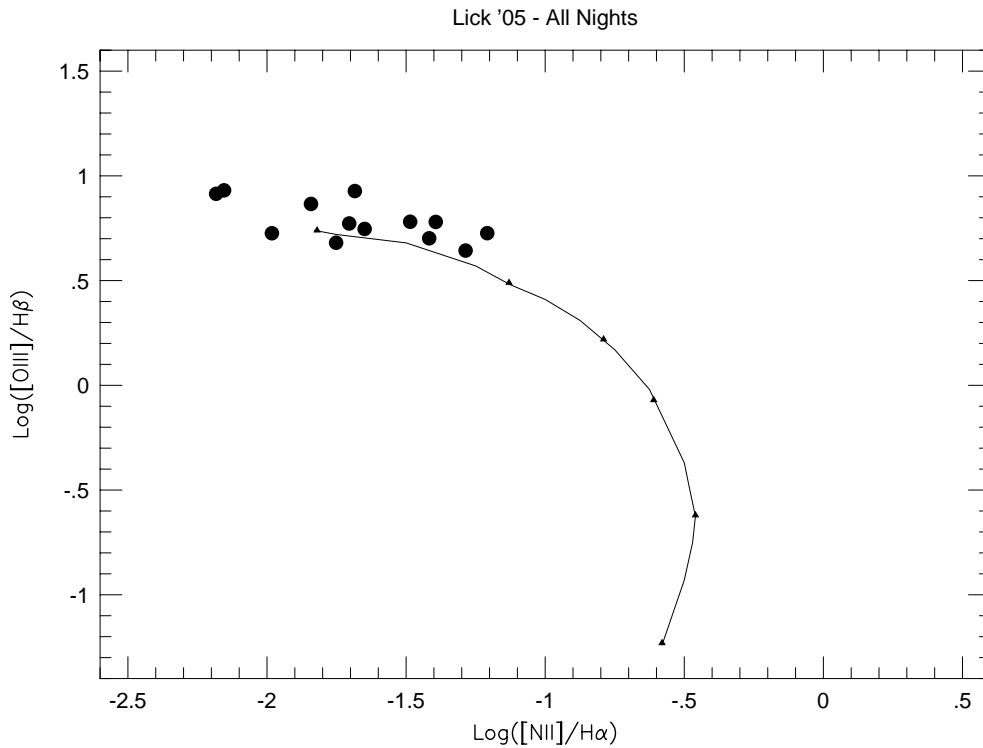


**Figure 4.2:** Diagnostic diagram for the 12 galaxies used in the nebular abundance sample. Filled circles are the 12 galaxies; the solid line represents the general shape of the diagnostic curve for emission-line galaxies.

The quantity  $\log(\text{O}/\text{H}) + 12$  is normally used to represent the general metal abundance of an emission-line galaxy. In our data, it ranges from 7.80 to 8.16. Analogous studies to this one have been carried out by Lee et al. (2004) and Melbourne et al. (2004) which found ranges of 7.61 to 8.32 and 7.50 to 8.05, respectively. The data obtained here show somewhat higher abundances than these other studies, but are generally consistent with their results. In particular, we did not find any galaxies with lower abundances than the minimum of the two other studies. Thus, despite our clear selection bias towards low-metallicity systems, we did not detect anything outside the established bounds for this type of data set.

Melbourne & Salzer (2002) carried out a large-scale survey of star-forming galaxy metallicities which did not specifically select for metal-poor systems. In comparison with the spread of  $\log(\text{O}/\text{H}) + 12$  they found, our answers here are towards the low end of the continuum. However, it is important to remember that the lowest-abundance galaxy ever observed, I Zwicky 18, has  $\log(\text{O}/\text{H}) + 12 = 7.17$ , according to Skillman & Kennicutt (1993). Clearly nothing found here, or in the other two studies mentioned above, approaches the limit set by I Zw 18. One of the goals of this work is to investigate why I Zw 18 appears to have such an anomalously low metal abundance. This data set is evidence for that, but this in itself is not a novel result. Many searches have been undertaken since the discovery of I Zw 18 to locate galaxies with similarly low abundances, and none have been successful. In Chapter 5, some data and theory attempting to explain this will be presented.

Source	$\lambda$ (Å)	KB9	KB17	KB18	KB27	KB53	KB74
[O II]	3727	195±11	175±10	180±12	93.2±5.77	144±11	200±13
[Ne III]	3869	36.9±2.69	49.2±2.94	46.0±3.52	36.6±2.55	43.4±3.62	49.1±3.69
[N III]	3970	...	27.1±1.68	...	36.6±2.49	20.3±2.25	31.5±2.50
H $\delta$	4101	41.4±2.21	25.3±1.48	27.7±2.16	28.1±1.81	26.2±2.26	30.1±2.18
H $\gamma$	4340	44.8±2.22	50.6±2.48	45.3±2.93	52.8±2.80	46.2±3.24	54.8±3.21
[O III]	4363	10.0±1.34	6.43±0.73	7.37±1.23	9.57±0.98	7.47±1.33	9.29±1.24
H $\beta$	4861	100±4.8	100±4.2	100±5.0	100±4.4	100±5.2	100±4.9
[O III]	4959	162±6	166±7	206±9	180±7	154±7	159±8
[O III]	5007	482±18	515±20	583±24	536±21	476±21	501±23
[N II]	6548	...	5.76±0.51	...	...	...	5.88±0.78
H $\alpha$	6564	286±3	284±6	282±4	290±6	279±5	297±8
[N II]	6584	6.26±1.01	18.5±0.96	9.16±0.87	3.03±0.50	4.94±1.15	11.4±0.85
[S II]	6716	21.7±1.39	12.7±0.73	16.3±1.32	6.01±0.53	17.3±1.27	16.9±1.27
[S II]	6731	19.5±1.36	14.1±0.75	13.1±0.90	8.01±0.78	10.7±1.19	14.2±0.90
[Ar III]	7136	...	...	...	...	...	8.64±0.77
C $\text{H}\beta$		0.02	0.34	0.32	0.18	0.10	0.40
log $F(\text{H}\beta)$		-14.41	-14.32	-14.73	-14.46	-14.79	-14.72
Absorption		4.0 Å	1.0 Å	2.0 Å	0.0 Å	1.0 Å	0.0 Å

**Table 4.1:** Scaled, corrected intensities of emission lines for blue survey objects normalized to the flux of H $\beta$

Source	$\lambda$ ( $\text{\AA}$ )	KR978	KR1555	KR1650	KR1735	KR1741	KR1814
[O II]	3727	123 $\pm$ 7	272 $\pm$ 15	51.3 $\pm$ 3.52	50.4 $\pm$ 4.01	156 $\pm$ 12	74.4 $\pm$ 4.42
[Ne III]	3869	43.0 $\pm$ 2.51	31.5 $\pm$ 2.05	69.1 $\pm$ 4.41	61.7 $\pm$ 4.26	55.9 $\pm$ 5.07	67.1 $\pm$ 3.86
He I + H8	3889	15.4 $\pm$ 1.54	14.4 $\pm$ 1.26	18.4 $\pm$ 1.94	17.2 $\pm$ 1.86	...	21.5 $\pm$ 1.45
[N III]	3970	27.3 $\pm$ 1.78	22.8 $\pm$ 1.62	36.9 $\pm$ 2.42	22.2 $\pm$ 2.31	...	37.5 $\pm$ 2.11
H $\delta$	4101	22.7 $\pm$ 1.59	25.8 $\pm$ 1.56	40.2 $\pm$ 2.56	24.5 $\pm$ 1.89	25.4 $\pm$ 2.94	25.3 $\pm$ 1.40
H $\gamma$	4340	53.3 $\pm$ 2.42	48.4 $\pm$ 2.35	48.9 $\pm$ 2.85	52.7 $\pm$ 3.06	50.4 $\pm$ 4.09	47.9 $\pm$ 2.35
[O III]	4363	8.35 $\pm$ 1.09	7.24 $\pm$ 0.70	15.8 $\pm$ 1.29	11.1 $\pm$ 1.62	9.56 $\pm$ 2.57	11.5 $\pm$ 0.93
H $\beta$	4861	100 $\pm$ 3.7	100 $\pm$ 4.2	100 $\pm$ 4.9	100 $\pm$ 3.7	100 $\pm$ 5.3	100 $\pm$ 4.5
[O III]	4959	192 $\pm$ 7	144 $\pm$ 6	244 $\pm$ 11	257 $\pm$ 11	179 $\pm$ 8	261 $\pm$ 11
[O III]	5007	605 $\pm$ 20	434 $\pm$ 17	740 $\pm$ 31	774 $\pm$ 31	561 $\pm$ 23	853 $\pm$ 36
[N II]	6548	...	4.12 $\pm$ 0.62	...	...	...	...
H $\alpha$	6564	284 $\pm$ 4	281 $\pm$ 5	307 $\pm$ 8	284 $\pm$ 5	281 $\pm$ 4	280 $\pm$ 7
[N II]	6584	11.5 $\pm$ 1.04	14.5 $\pm$ 0.91	4.43 $\pm$ 1.03	1.85 $\pm$ 0.91	5.52 $\pm$ 1.77	5.79 $\pm$ 0.58
[S II]	6716	12.5 $\pm$ 1.04	28.1 $\pm$ 1.31	4.20 $\pm$ 1.03	13.5 $\pm$ 1.27	12.1 $\pm$ 1.76	5.78 $\pm$ 0.58
[S II]	6731	5.42 $\pm$ 1.01	18.2 $\pm$ 0.97	7.12 $\pm$ 1.05	4.32 $\pm$ 0.91	8.24 $\pm$ 1.74	4.01 $\pm$ 0.56
[Ar III]	7136	...	...	...	...	...	...
$c_{\text{H}\beta}$		0.04	0.06	0.09	0.22	0.32	0.01
$\log F(\text{H}\beta)$		-14.54	-14.32	-14.74	-14.56	-14.88	-14.44
Absorption		2.0 $\text{\AA}$	1.0 $\text{\AA}$	0.0 $\text{\AA}$	2.5 $\text{\AA}$	1.5 $\text{\AA}$	0.0 $\text{\AA}$

Table 4.2: Scaled, corrected intensities of emission lines for red survey objects normalized to the flux of H $\beta$

Parameter	KB9	KB17	KB18	KB27	KB53	KB74
$T_{e,[O III]}$ (K)	15614±979	12569±539	12647±797	14527±639	13783±1009	14813±871
$T_{e,[N II]}$ (K)	13884±387	12535±268	12573±394	13488±273	13110±457	13559±365
$N_e$ (cm <sup>-3</sup> )	379±176	906±215	177±146	1737±726	100	253±144
$O^+/H^+ \times 10^{-5}$	1.92±0.28	3.16±0.37	2.80±0.46	1.33±0.19	1.78±0.33	2.15±0.32
$O^{2+}/H^+ \times 10^{-5}$	4.39±0.78	8.85±1.30	9.89±2.01	5.95±0.82	6.23±1.41	5.28±0.95
$O/H \times 10^{-5}$	6.31±1.05	12.0±1.6	12.7±2.4	7.27±0.97	8.01±1.73	7.44±1.24
$N^+/H^+ \times 10^{-7}$	4.83±0.95	21.1±2.0	10.3±1.6	2.69±0.50	4.76±1.29	9.64±1.28
$N/H \times 10^{-6}$	1.59±0.35	8.04±1.11	4.67±0.91	1.48±0.32	2.13±0.64	3.33±0.56
$S^+/H^+ \times 10^{-7}$	3.99±0.51	4.20±0.40	3.96±0.52	1.93±0.31	3.18±0.49	3.21±0.40
$S/H \times 10^{-7}$	4.53±0.59	4.85±0.48	4.67±0.65	2.34±0.36	3.75±0.59	3.67±0.47
$\log(O/H) + 12$	7.80±0.06	8.08±0.05	8.10±0.08	7.86±0.06	7.90±0.09	7.87±0.07

**Table 4.3:** Nebular abundances and other physical parameters for blue survey objects.

Parameter	KR978	KR1555	KR1650	KR1735	KR1741	KR1814
$T_{e,[O III]}$ (K)	13085±664	14146±571	15714±603	13273±769	14270±1641	12966±400
$T_{e,[N II]}$ (K)	12786±317	13272±251	13924±237	12875±362	13327±716	12729±193
$N_e$ (cm <sup>-3</sup> )	100	100	4293±5051	100	100	100
$O^+/H^+ \times 10^{-5}$	1.73±0.22	3.16±0.33	0.785±0.359	0.683±0.106	1.77±0.49	1.07±0.10
$O^{2+}/H^+ \times 10^{-5}$	9.27±1.49	5.25±0.69	6.59±0.79	11.3±2.1	6.62±2.26	13.4±1.5
$O/H \times 10^{-5}$	11.0±1.7	8.41±0.99	7.37±0.98	12.0±2.2	8.39±2.74	14.5±1.6
$N^+/H^+ \times 10^{-7}$	12.2±1.6	13.3±1.3	3.53±0.89	1.90±0.97	4.99±1.93	6.23±0.73
$N/H \times 10^{-6}$	7.74±1.26	3.55±0.43	3.31±1.34	3.35±1.76	2.37±1.00	8.47±1.24
$S^+/H^+ \times 10^{-7}$	2.23±0.28	5.02±0.44	1.84±0.93	2.17±0.31	2.17±0.54	1.24±0.13
$S/H \times^{-7}$	2.75±0.36	5.55±0.50	2.40±1.08	3.20±0.48	2.58±0.65	1.73±0.19
$\log(O/H) + 12$	8.04±0.06	7.92±0.05	7.87±0.05	8.08±0.07	7.92±0.12	8.16±0.05

Table 4.4: Nebular abundances and other physical parameters for red survey objects.

## 4.5 Comparison of ELSA with Prior Results

As a means of checking ELSA's consistency with the existing canon of results for nebular abundance studies, a side-by-side comparison between ELSA results and previously published results was carried out. For this comparison, two KISS galaxies were selected, one from each survey: KISSB 86 and KISSR 286. A full run of nebular abundances has been published for these galaxies in Lee et al. (2004). The observing parameters and initial reductions for these targets are identical to those described in §4.2-3. The previously published abundances were derived using the NEBULAR package in IRAF.

Exact agreement between ELSA and the published abundances is not expected, as ELSA uses more recent atomic constants than NEBULAR, which produced the abundance results in Lee et al. However, we do find that ELSA's answers are quite similar – nearly always within the formal errors – to the published results. The primary exception is in the S/H sulfur abundance. This is most likely due to differences in the handling of the ionization correction factor for sulfur, which has historically proven difficult to calibrate. In this particular study, the O/H oxygen abundance is of paramount importance for reasons explained earlier in this chapter. The results here are encouraging, as ELSA obtained answers which agree within the formal errors. This indicates both that prior methods for obtaining the O/H abundance and the subsequent answers are generally reliable, and that ELSA produces reliable answers as well.

Parameter	KB86		KR286	
	ELSA	Published	ELSA	Published
$T_{e,[O III]}$ (K)	12482±206	12390±382	11066±177	11010±298
$N_e$ (cm <sup>-3</sup> )	100	100	30.3±32.96	100
$O^+/H^+ \times 10^{-5}$	3.24±0.15	3.40±0.18	4.13±0.20	3.99±0.21
$O^{2+}/H^+ \times 10^{-5}$	7.70±0.49	8.09±0.88	10.9±0.7	10.9±1.2
$O/H \times 10^{-5}$	10.9±0.6	11.5±0.9	15.0±0.8	14.9±1.2
$N^+/H^+ \times 10^{-7}$	12.1±0.6	13.0±0.4	21.4±0.9	20.2±0.7
$N/H \times 10^{-6}$	4.08±0.26	4.40±0.47	7.78±0.47	7.55±0.85
$S^+/H^+ \times 10^{-7}$	5.20±0.2	5.66±0.17	5.94±0.23	5.89±0.18
$S/H \times 10^{-7}$	19.3±2.8	...	26.0±2.0	31.3±3.0

**Table 4.5:** Comparison of published abundances from Lee et al. (2004) with abundances produced by ELSA.

# Chapter 5

## The Volume Density-Abundance Relationship

### 5.1 The Coarse Abundance Method

In Chapters 1 and 4, we discussed the perplexing case of I Zwicky 18, the lowest-abundance galaxy ever discovered. I Zw 18 has been known for over 30 years, during which time a vast number of nebular abundance studies have been done, many of which were deliberately attempting to locate low-metallicity galaxies with O/H on the order of I Zw 18. None have been successful. KISS certainly has the sensitivity to detect galaxies with luminosities as low as I Zw 18's metallicity would imply, yet as one can see from the discussion of the results in Chapter 4, followup nebular abundance studies consistently show that nothing with an abundance approaching that of I Zw 18 has been found. This chapter will investigate the relationship between metallicity (as given by O/H) and the volume density of

galaxies.

Building a statistical relationship such as the one between metallicity and volume density requires a large number of data points. In Chapter 4, nebular abundances for a sample of 12 galaxies taken from the KISS data set were presented. Although this is a critical step in obtaining a statistically significant set of data points, it in itself is not sufficient. To obtain a large enough data set, we use both the strong line and coarse abundance methods, which were briefly described in Chapter 4.

True nebular abundances are only possible if a reliable estimate of the electron temperature, density and line emissivity (i.e., excited state level population) can be found. In practice, the temperature proves to be the most elusive of these quantities. Determining the temperature depends on the availability of multiple lines from either the [O III] or [N II] spectrum. However, for the large majority of galaxies observed in KISS followup studies, no estimate of the temperature is possible since the [O III]  $\lambda 4363$  line is not detectable. Recall also that the [N II]  $\lambda 5755$  line is almost never detectable in emission-line galaxy spectra even in the best of circumstances. This leaves us with no direct means of obtaining the temperature, and thus no means of computing nebular abundances.

The strong line and coarse methods are essentially a “back-up plan” for cases like this where nebular abundances are not an option. In the event that  $\lambda 4363$  is not detected, but the [O II]  $\lambda 3726/\lambda 3729$  lines are, it is possible to use the strong line or  $R_{23}$  method. This method involves finding the value of a parameter known

as  $R_{23}$  using the observed data. The parameter is defined as

$$R_{23} = \frac{F(\lambda 4959 + \lambda 5007) + F(\lambda 3726 + \lambda 3729)}{F(\text{H}\beta)}. \quad (5.1)$$

The first term of the numerator incorporates the two main lines resulting from downward transitions from the (singlet) first excited state into the (triplet) ground state for the  $\text{O}^{2+}$  ion, and the second term incorporates the two transitions from the (doublet) first excited state to the (singlet) ground state for the  $\text{O}^+$  ion. Once again, oxygen is chosen as the surrogate for general metallicity since both of its major ionization stages may be observed in the visible part of the spectrum.

Typically the strong line method is calibrated by finding  $R_{23}$  for a sufficiently large sample of galaxies where nebular abundances have already been derived, and obtaining whatever fit is appropriate for the data. Melbourne & Salzer (2002) describe obtaining this fit using a sample of KISS nebular abundances, supplemented with data from the literature. They found that the relationship between total oxygen abundance – which is usually expressed in the form  $\log(\text{O}/\text{H}) + 12$  – and  $\log(R_{23})$  is double valued, with an upper and lower branch (see below). Both branches showed a linear relationship between  $\log(\text{O}/\text{H}) + 12$  – and  $\log(R_{23})$ , although with very different slopes.

The last resort in the event that the [O II] lines are not available is the coarse method. In this case, a relationship is established only between the ratio of either [O III]  $\lambda 5007/\text{H}\beta$  or [N II]  $\lambda 6583/\text{H}\alpha$  to the value of  $\log(\text{O}/\text{H}) + 12$ . The ratios used in the coarse method are mostly immune to reddening effects since they lie close to each other in wavelength. The coarse method is calibrated in a similar

fashion to the  $R_{23}$  method. Existing abundance data (either nebular or  $R_{23}$  in origin) is plotted against one of the two ratios mentioned above, and a fit is obtained.

An additional complicating factor in both the coarse method and the strong line method is that emission-line galaxies can be divided into two distinct “branches” of metallicity. The difference between these branches can be seen on the diagnostic diagram shown in Figure 5.1. The “upper branch” of the diagram represents more massive and luminous galaxies with higher metal abundances (found in the lower right portion of the diagram). It is almost entirely insensitive to  $[\text{N II}] \lambda 6583/\text{H}\alpha$ . The lower branch (found in the upper left portion of the diagram) is insensitive to  $[\text{O III}] \lambda 5007/\text{H}\beta$ . In these cases, the more sensitive line ratio alone is used for coarse abundance calculations. For the transitional region between the two branches, a weighted mean of the line ratios is used.

As it were, 12 galaxies for which nebular abundances have been calculated is not enough to calibrate either the  $R_{23}$  method or the coarse method accurately. The data points discussed in this chapter are all coarse abundances derived from previous observations of KISS dwarf galaxies, except for a set of 38 galaxies where nebular abundances were calculated (see below).

## 5.2 Determining Volume Density

Once a large collection of data points has been assembled, the next step in determining the abundance-volume density relationship is to create bins of abundances and obtain volume densities for them. The sample we used for carrying

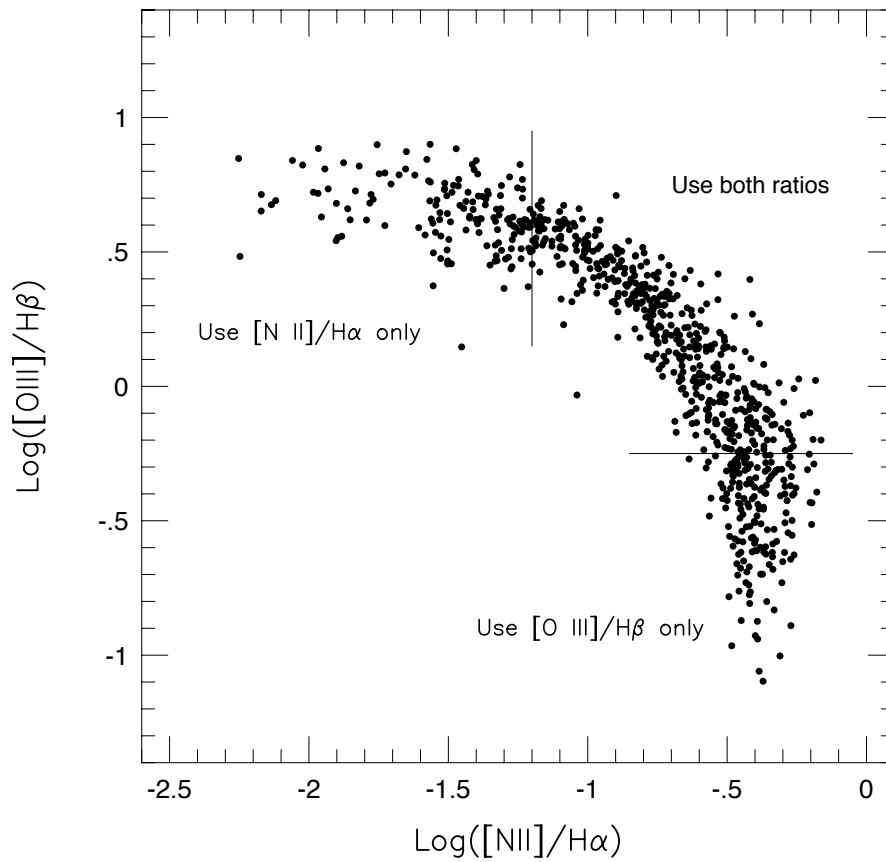


**Figure 5.1:** Diagnostic diagram showing the two branches and the transitional region. All points shown are from the data set described in §5.2.

out this process consisted of 781 galaxies with estimated abundances less than  $\log(\text{O}/\text{H}) + 12 = 8.70$ . Of these 781, 12 were from the data set discussed in Chapter 4. Another 26 were taken from the nebular abundance studies referenced in Chapter 4: Lee et al. (2004) and Salzer et al. (2004). The remaining targets were all coarse abundances taken from Melbourne & Salzer (2002) and Salzer et al. (2005).

When the KISS survey was first carried out, redshifts were obtained for all galaxies catalogued. Therefore, the distance to any KISS galaxy selected for followup observation can be found trivially using Hubble's law:

$$cz = H_0 d \quad (5.2)$$

where  $H_0$  is the Hubble constant (currently thought to be about  $70 \text{ km s}^{-1} \text{ Mpc}^{-1}$ ) and  $d$  is the distance to the galaxy, in Mpc. The redshift  $z$  is given as a dimensionless fraction of the speed of light  $c$ .

When any value of  $d$  is known, it is straightforward to obtain the volume of space within which it could be detected. The volume is given by:

$$V_{\text{max}} = \frac{4}{3} \pi d_{\text{max}}^3 A_{\text{sky}} \quad (5.3)$$

where  $A_{\text{sky}}$  is the fraction of the sky sampled by the survey area. All 781 galaxies in the sample have strong lines ( $\text{H}\alpha$  for the red survey, and  $[\text{O III}] \lambda 5007$  for the blue survey) which are above the completeness limit (as defined in Chapter 4, the limit below which full detection of all objects cannot be guaranteed). Thus, we only include in our sample objects above the completeness limit, making our

sample statistically valid.

Next, the *line luminosity* is determined. This is done with the standard distance modulus, which is defined in terms of magnitudes as

$$m_l - M_l = 5 \log \left( \frac{d}{10 \text{ pc}} \right) \quad (5.4)$$

where  $m_l$  and  $M_l$  are the line flux and luminosity, respectively, expressed in magnitude units, such that

$$m_l = -2.5 \log F_l + C \quad (5.5)$$

and

$$M_l = -2.5 \log L_l + C \quad (5.6)$$

where  $C$  is a constant which adjusts the raw log of the flux or luminosity to the standard magnitude scale.

Since the distance  $d$  is known, the value of  $M_l$  can be computed. The same equation is then used to determine  $d_{\text{max}}$ , the maximum distance at which an galaxy with this value of  $M_l$  can be detected. This is accomplished by setting  $m_l$  in Equation (5.4) to be the magnitude of the KISS completeness limit. The maximum sample volume  $V_{\text{max}}$  is determined using Equation (5.3).

All galaxies in the sample were placed into one of 11 bins of abundance. Each bin spanned 0.1 dex (where 1 dex is a difference of 1 in terms of  $\log(\text{O}/\text{H})+12$ ), for a total range of 1 dex. Finally, the volume density of galaxies with the abundance

specified by each bin was determined using the equation:

$$\rho = \sum_{i=1}^N \frac{1}{V_i} \quad (5.7)$$

where  $N$  is the number of galaxies placed into the bin in question, and  $V_i$  represents the maximum detection volume of galaxy  $i$ .

Of the 781 objects in the sample, 389 came from the survey strip at  $30^\circ$  declination and the other 392 from the  $43^\circ$  declination strip. An independent volume density was calculated for each bin in each survey, and a formal error was determined such that:

$$\sigma_\rho = \frac{\sqrt{N}}{N} \rho \quad (5.8)$$

The volume densities for each survey strip were used to compute a final average volume density for each abundance bin by taking a weighted mean and weighted formal error in the mean, along the lines of Equations (3.8) and (3.9). These were the final measurements used to establish the volume density-abundance relationship.

### 5.3 Results

What follows is a table of the weighted mean volume densities with errors for each bin of abundance in terms of  $\log(\text{O}/\text{H}) + 12$ , shown as Table 5.1. The mean abundance for each bin was assumed to be the middle value of the range; had actual mean abundances been calculated, they would not have been very far from these middle values. A plot of the data is also included, with error bars, shown

as Figure 5.2. Note that the data point at 8.15 dex was omitted from the plot. This is due to a systematic error in the coarse abundance method that occurs for objects between  $\log(\text{O}/\text{H}) + 12$  of 8.1 and 8.2. This is explained further in Salzer et al. (2005).

The graph in Figure 5.2 begins at extremely low volume densities for abundances between 7.60 and 7.80 dex, and quickly grows by more than a factor of 20 by 8.20 dex. The graph levels off beyond 8.20 dex, with data points mostly agreeing with one another within the errors. Out of the entire sample of 781 galaxies, none had  $\log(\text{O}/\text{H}) + 12 < 7.60$ , which is quite telling. The average  $d$  for the 7.65 dex bin (found by taking  $cz/H_0$ ) is 233 Mpc, which is well within the detection limit of KISS. KISS also has the sensitivity to detect very low luminosity systems, so the parameters of the survey does not at all preclude detection of low luminosity systems. This means that any extremely low abundance galaxies which are present in the local Universe (out to the redshift limit of KISS) ought to have been detected. Yet, they were not. For this reason, it is not clear from this particular data set how the volume density-abundance relationship would behave at even lower values of  $\log(\text{O}/\text{H}) + 12$ .

This certainly has implications for understanding the lack of very low abundance systems detected in studies such as this one. It is also worth noting that despite the success of this study in showing a positive correlation between metallicity and volume density, the size of the sample here is still what could be considered small for the task at hand. The noisiness of the graph could further be reduced by using an even larger sample of galaxies.

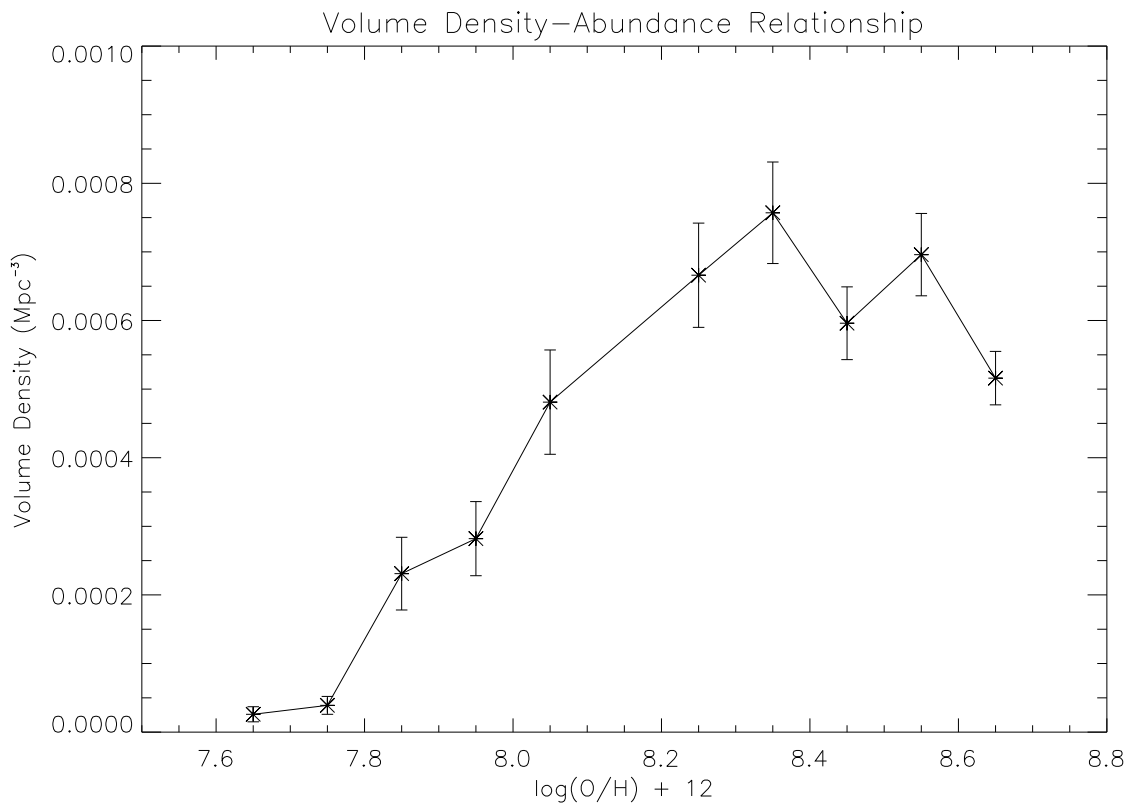


**Figure 5.2:** Plot of the weighted mean volume strips using data shown in Table 5.1.

Abundance Bin	Mean Abundance	# Objects	Density ( $\text{Mpc}^{-3}$ )
7.60-7.70	7.65	8	$0.000026 \pm 0.000011$
7.70-7.80	7.75	10	$0.000039 \pm 0.000013$
7.80-7.90	7.85	19	$0.000231 \pm 0.000053$
7.90-8.00	7.95	30	$0.000282 \pm 0.000054$
8.00-8.10	8.05	43	$0.000481 \pm 0.000076$
8.10-8.20	8.15	27	$0.000072 \pm 0.000017$
8.20-8.30	8.25	76	$0.000666 \pm 0.000076$
8.30-8.40	8.35	104	$0.000757 \pm 0.000074$
8.40-8.50	8.45	135	$0.000596 \pm 0.000053$
8.50-8.60	8.55	154	$0.000696 \pm 0.000060$
8.60-8.70	8.65	175	$0.000516 \pm 0.000039$

**Table 5.1:** Weighted mean volume densities across the  $30^\circ$  and  $43^\circ$  bands in declination from the KISS survey.

## 5.4 Discussion

As discussed in Chapter 1, part of the motivation for investigating the volume density-abundance relationship was to attempt to explain the relative paucity of galaxies with abundances similar to I Zwicky 18, and why despite concerted efforts to find similar objects, none have been discovered. As Figure 5.2 shows, galaxies with  $\log(\text{O}/\text{H}) + 12 < 8.00$  become increasingly rare. Low metallicity galaxies, with  $\log(\text{O}/\text{H}) + 12 < 7.50$  would occur with dramatically lower volume density than galaxies at higher metallicities. This would suggest that the uniqueness of I Zw 18 ( $\log(\text{O}/\text{H}) + 12 = 7.17$ ) has an empirical basis, even if the physical reason for it is not entirely clear.

Observations of neutral hydrogen in low luminosity systems which do not exhibit emission line features (i.e., which are not active star-forming galaxies) have

shown that a number of them are, in fact, gas-rich; they have the raw materials to begin star formation. Yet, as the results of this thesis show, there does not appear to a corresponding cohort of low luminosity, metal-poor star-forming galaxies. In fact, there is a rather severe lack of them. One explanation for this may be that the result obtained here and in other studies is erroneous and we simply unable to detect the low metallicity galaxies for some reason. This seems unlikely due to the aforementioned sensitivity of KISS, which should have been able to detect low metallicity systems if they existed.

Another explanation is that the lack of low metallicity systems is a result of the nature of galaxian chemical evolution. It has been suggested by a number of authors, including Kunth & Sargent (1983), that galaxies composed of pure, unenriched hydrogen gas transition rapidly from that phase to a higher threshold level of O/H abundance. While the results shown in Figure 5.2 are preliminary, it may be that the “level off” rate of about 8.0 to 8.2 dex in the plot does in fact represent that threshold. This would further suggest that the few galaxies we do find with O/H abundance below that threshold are either very young galaxies which we have been fortunate enough to catch in the midst of their (presumably very short) transition from pure gas to the threshold level, or that they are systems whose abundances has been effected by some external process, such as infall of unenriched gas which dilutes it to a lower abundance.

Regardless of the physical causes of it, the relationship shown in Figure 5.2 is a highly significant result which has never been previously demonstrated in this empirical, statistical fashion. There is still a great deal of work to be done to refine and further explore the issues raised in this chapter, but the volume density-

abundance correlation is nonetheless an important piece of the puzzle with regards the currently accepted model of chemical abundances and chemical evolution in low-mass galaxies.

# Chapter 6

## Conclusion

This thesis has focused on three main goals:

1. updating and adapting ELSA to process extragalactic data such as that from emission-line galaxies,
2. obtaining direct nebular abundances with ELSA for a sample of recently observed galaxies from KISS which are thought to be low-abundance, and
3. using a large data set comprised of both nebular and coarse abundances to investigate whether there is a correlation between metallicity and volume density, with an eye towards empirically characterizing the uniqueness of extremely low abundance systems like I Zwicky 18.

We have introduced ELSA as a tool to find nebular abundances, and described the scientific justification and operational aspects of the program, including the temperature and density calculations, the dereddening and absorption correction process, and the physical model used to obtain the abundances.

As shown in §4.5, ELSA measures up quite well as a tool for abundance work. It integrates all the steps of producing nebular abundances from measured line fluxes to improve the efficiency and accuracy of the abundance process while still providing answers which agree with existing published results. ELSA holds great promise facilitating a much faster turnaround for a nebular abundance data set, in addition to keeping all atomic data updated to the latest versions available.

ELSA was used to find nebular abundances for 12 galaxies selected from the KISS database. These galaxies were selected for [O III]  $\lambda 4363$  observability, a criteria which ensures that they are usable candidates for nebular abundances, but which at the same time predicts that they will be low abundance systems. Despite this selection effect, no galaxies were found with extremely low abundances ( $\log(O/H) + 12 < 7.5$ ). As this study involves a statistically complete sample of galaxies, it further reinforces the notion that the extreme rareness of I Zw 18 has an empirical and therefore physical basis.

After combining the nebular abundances we found with other sets of nebular abundances and a large number of coarse abundances, a volume density-abundance plot was created. It showed a striking relationship between volume density and metallicity, suggesting that there is a threshold O/H abundance level below which the volume density becomes very low very quickly – that is to say, galaxies with that abundance are extremely rare. This would seem to lend credibility to the idea that chemical enrichment is a very rapid process that begins soon after star formation begins and quickly reaches the aforementioned threshold level.

There is still much work to be done on all these fronts. A large backlog of abundance quality spectra exists. ELSA will be instrumental in finding nebular abundances for these objects in a reasonable time frame. With a sizable pool of nebular abundances, a recalibration of the coarse method (see §5.1) will be possible, improving the accuracy of the data points used to produce Figure 5.2. More data and a more robust coarse abundance model will produce even higher quality results.

It is only since the advent of KISS that it has been possible to carry out this type of project with such a large sample size, and the results as more data are added will be exciting and enlightening. The result of the volume density-abundance relationship will hopefully prove to be an important step in understanding galaxian chemical evolution and star formation processes in the future.

# References

- Aller, L. H. 1984, *Physics of Thermal Gaseous Nebulae* (Boston: D. Reidel Publishing)
- De Robertis, M. M., Dufour, R. J., & Hunt, R. W. 1987, JRASC, 81, 195.
- Indebetouw, R. et al. 2005, ApJ, 619, 931.
- Izotov, Y. I., Thuan, T. X., & Lipovetsky, V. A. 1994, ApJ, 435, 647.
- Kunth, D., & Sargent, W. L. W. 1983, ApJ, 273, 81.
- Kwitter, K. B., & Henry, R. B. C. 2001, ApJ, 562, 804.
- Lee, J. C., Salzer J. J., Impey, C., Thuan, T. X., & Gronwall, C. 2002, AJ, 124, 3088.
- Melbourne, J., Phillips, A., Salzer, J. J., Gronwall, C., & Sarajedini, V. L. 2004, AJ, 127, 686.
- Melbourne, J., & Salzer, J. J. 2002, AJ, 123, 2302.
- Osterbrock, D. E., & Ferland, G. J. 2006, *Astrophysics of Gaseous Nebulae and Active Galactic Nuclei* (Sausalito: University Science Books).
- Pagel, B. E. J., Simonson, E. A., Terlevich, R. J., & Edmunds, M. G. 1992, MNRAS, 255, 325.
- Rieke, G. H., & Lebofsky, M. J. 1985, ApJ, 288, 618.
- Salzer J. J. et al. 2000, AJ, 120, 80.
- Sargent, W. L. W., & Searle, L. 1970, ApJ, 162, L155.
- Savage, B. D., & Mathis, J. S. 1979, ARA&A, 17, 73.
- Seaton, M. J. 1979, MNRAS, 187, 73.
- Skillman, E. D., & Kennicutt, R. C. 1993, ApJ, 411, 655.

Stasinska, G. 1990, A&AS, 83, 501.

Storey, P. J., & Hummer, D. G. 1995, MNRAS, 272, 41.